Contents

List of Figures

List of Tables

Todo list

Chapter 1

Secrets of the nature

In this chapter, we will try to understand the world surrounding us thanks to a mathematical framework which describes the matter and its interaction. We will first have a look at the laws that lead our Universe. Then, we will focus on the mathematical framework with the description of three interactions: the electromagnetism, the weak and the strong interactions. After that, we will study the electroweak interaction and the spontaneous symmetry breaking. We will finally discuss the limits of the theory and the solutions to avoid the limits.

Contents

1.1 The Standard Model

1.1.1 Introduction

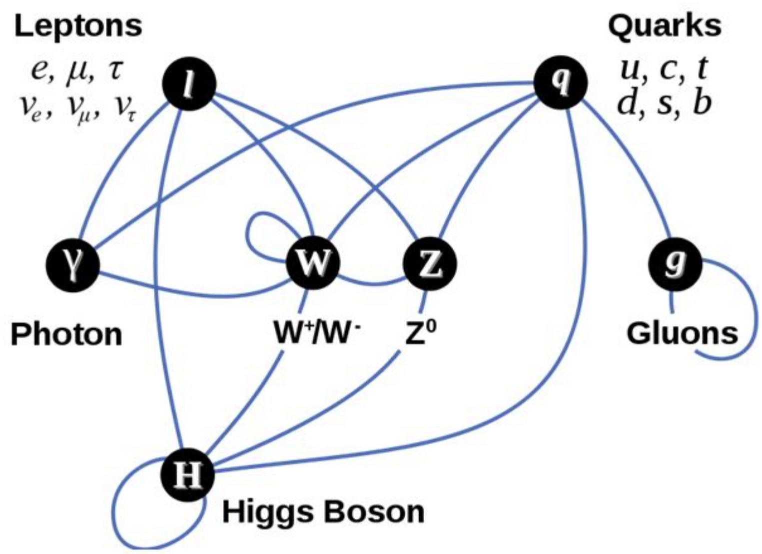

Figure 1.1 – Summary of the Standard Model particles with their interactions. http://www.brighthub.com/science/space/articles/84750.aspx

The Standard Model (SM) is a theory that describes the elementary structure of the matter surrounding us. It is one of the most successful achievements in modern physics. The elegant theoretical framework of the Standard Model (SM) is able to provide good explanations of experimental results but is also able to predict a wide variety of phenomena.

The SM depicts the interactions between the fundamental constituents of matter, called particles. From a quantum point of view, a particle is defined by its intrinsic angular momentum, called spin. This quantum number is a key to distinguish between the particles of 'matter' and the 'carrier force' particles.

The half integers spin particles are obeying to the Fermi-Dirac statistics and are submitted to the Pauli exclusion principle: they can not occupy the same quantum state at the same time. These particles are called fermions. They are the constituents of the matter and are to the number of twelve.

The fermions are divided into two categories: the leptons and the quarks. The leptons are to the number of six: three charged particles and three neutral particles called neutrino. The first fundamental particle discovered in particle physics was the electron (e^-) at the end of the 19^{th} century. The two other charged leptons were discovered in 1937 for the muon (μ) and in 1975 for the tau (τ). Three neutrinos are associated to the three flavored leptons: the electron neutrino (ν_e) discovered in 1953, the muon neutrino (ν_μ) in 1962 and the tau neutrino (ν_τ) discovered in 2000.

The quarks are to the number of six. They can't be found alone in nature. They are carrying a quantum number: the color. The color quantum numbers are green, blue and red (and the anti-color associated). They are always in a bounded state to form composite particles that are colorless and are called hadrons. A quark and an anti-quark form an integer spin composite particle, a meson. Three quarks bounded together are called baryons. The most known baryons are the proton and the neutron. They are made of the up quarks (u) and the down quarks (d). The other quarks were discovered in the second half of the 20^{th} century. The strange quark (s) was discovered in 1968, followed by the charm quark (c) in 1974. Then, the bottom quark or beauty quark (b) was discovered in 1977. The last quark discovered was the top quark (t) in 1995.

The fermions are also divided into three categories which depend on the mass of the particle. They are called generations. The first generation of particles is composed of the electron, the electron neutrino, the u and d quarks. They form the ordinary matter. The two other generations are particles found in cosmic rays or in collisions with accelerators. All the fermions and their properties are summarised in the table 1.1.

Conservation laws and invariance

The second kind of particles are integer spins particles and are labelled bosons or gauge bosons. They are following the Bose-Einstein statistics. It means that the bosons are not limited to a single occupancy of the same state as the fermions. The bosons are the mediators of the four fundamental interactions.

The electromagnetic interaction (EM) is mediated by the photon γ, a massless and chargeless particle of spin 1. The EM is responsible for the interaction between two charged particles. The weak interaction which is responsible for the β radioactive decay (a nucleon is able to transform into

Type	Family	Particle	L	B	Q_e	Mass (MeV)
Leptons	1^{st}	e	1	0	-1	0.511
		ν_e	1	0	0	$< 2 \times 10^{-6}$
	2^{nd}	μ	1	0	-1	105.66
		ν_μ	1	0	0	$< 2 \times 10^{-6}$
	3^{rd}	τ	1	0	-1	1.78×10^3
		ν_τ	1	0	0	$< 2 \times 10^{-6}$
Quarks	1^{st}	u	0	1	2/3	$2.3^{+0.7}_{-0.5}$
		d	0	1	-1/3	$4.8^{+0.5}_{-0.3}$
	2^{nd}	s	0	1	-1/3	95 ± 5
		c	0	1	2/3	$1.275 \times 10^3 \pm 2.5$
	3^{rd}	b	0	1	-1/3	$4.66 \times 10^3 \pm 30$
		t	0	1	2/3	$173.21 \times 10^3 \pm 511 \pm 711$

Table 1.1 – Summary of the 12 fermions. L is a quantum number associated to the leptons. Its value is 1 for leptons and -1 for anti-leptons. B is a quantum number associated to the baryons. It is equal to 1 for a baryon and to -1 for an anti-baryon. [24]

an other one with the emission of a lepton and a neutrino). The gauge bosons associated with the weak interaction are the neutral electrical charged boson Z^0, and two electrical charged one W^+ and W^-. The strong interaction is mediated by eight gauge bosons, the gluons. It is responsible for the nucleus and the hadrons cohesion. The last force is the gravitational interaction but it is not included into the SM. Trying to find a framework where the equation of the general relativity used to describe the macro world and the equation of the quantum mechanics describing the micro world is a difficult challenge. From a quantum theory, the boson associated with the gravitational force might be the graviton, a spin 2 particle.

The Higgs boson (H) is a particle predicted by the S.M and has been discovered in 2012 at the Large Hadron Collider (LHC) It is the gauge boson of the Higgs mechanism. This mechanism is the mass generator of particles and will be presented later in section 1.2.2.

The table 1.2 summarises the different bosons of the SM.

Force	Gauge bosons	Mass (GeV/c^2)	Electric charge	Range
Electromagnetic	γ	0	0	∞
Weak	Z^0	91.1876 ± 0.0021	0	10^{-18} m
	$W^{\pm}$	80.3980 ± 0.0250	±1	
Strong	g (8 gluons)	0	0	10^{-15} m
	H	125 GeV	0	

Table 1.2 – Summary of the interactions and the boson defined by the Standard Model. [24]
N.B.: the graviton was not included in this table because the gravitational force is not taken into account in the SM.

1.1.2 Quantum Field Theory

The mathematical basis of the SM is the Quantum Field Theory (QFT). All the interactions are described by the gauge group:

$$SU_C(3) \otimes SU_L(2) \otimes U_Y(1) \tag{1.1}$$

The gauge theory is invariant under a continuous set of local transformation. Taking the gauge symmetries and the least action into account, physicists were able to set up equations that describe the dynamic of the interactions by Lagrangian. The steps to build Lagrangian for the three forces and the unification of the EM and weak interactions are going to be presented.

Quantum Electrodynamic

The Quantum Electrodynamic (QED) is the QFT that combines the electromagnetism formalism and the quantum mechanics formalism to describe the interaction thanks to a relativistic Lagrangian. As the charge Q_e of the electron is invariant on every part of the Universe, the QED Lagrangian should be invariant under some transformations. The $U(1)$ gauge group is a unitary group of one dimension which is invariant under space transformations.

Lets first consider the Dirac Lagrangian for a free fermion:

$$\mathcal{L}_{Dirac} = \overline{\Psi}(x)\left(i\gamma^{\mu}\partial_{\mu} - m\right)\Psi(x) \tag{1.2}$$

The Lagrangian is invariant under global U(1) transformation:

$$\begin{array}{rcl} \Psi(x) & \rightarrow & \Psi'(x) = e^{-i\alpha}\Psi(x) \\ \overline{\Psi}(x) & \rightarrow & \overline{\Psi}'(x) = e^{i\alpha}\overline{\Psi}(x) \end{array} \tag{1.3}$$

The corresponding local symmetry is:

$$\begin{array}{rcl} \Psi(x) & \rightarrow & \Psi'(x) = e^{-i\alpha(x)}\Psi(x) \\ \overline{\Psi}(x) & \rightarrow & \overline{\Psi}'(x) = e^{i\alpha(x)}\overline{\Psi}(x) \end{array} \tag{1.4}$$

Although the mass term of the Lagrangian in the equation 1.2 stays invariant under the local symmetry, the term containing a partial derivative is not anymore. A gauge field A_μ has to be added to the derivative to keep it invariant under local gauge transformation. The covariant derivative will be then:

$$D_\mu \Psi(x) = (\partial_\mu - iQ_e A_\mu)\Psi(x) \tag{1.5}$$

The gauge field is not yet a dynamic field. To get a physical gauge field, a kinetic term should be added to the equation. This gauge invariant term that includes derivative from the A_μ field is:

$$F_{\mu\nu} = \partial_\mu A_\nu - \partial_\nu A_\mu \tag{1.6}$$

The Lagrangian, which is local invariant, is the one that describes the QED:

$$\mathcal{L}_{QED} = \overline{\Psi}(x)(i\gamma^\mu D_\mu - m)\Psi(x) - \frac{1}{4}F_{\mu\nu}(x)F^{\mu\nu}(x) \tag{1.7}$$

A mass term $mA_\mu A^\mu$ for the field A_μ is missing because it is not gauge invariant. That consideration matches to the fact that the photon is a massless boson.

Add details on the QED: coupling...

Weak interaction

In 1930, Pauli assumed that the continuous energy spectrum of the electron in the β decay could be explained by the existence of a new particle to respect the principle of energy conservation. It is a light particle, which does not interact so much with matter.

After the discovery of the neutron by Chadwick in 1932, Fermi wrote a theory on weak interaction to explain the β decay. [13] He postulated that the neutron is decaying into a proton by emitting an electron and a light neutral particle, called neutrino. In analogy to the electromagnetism, he proposed a current-current Lagrangian to describe the β decay.

$$\mathcal{L}_{weak} = \frac{G_F}{\sqrt{2}} \left(\overline{p}\gamma_\mu n\right) \left(\overline{e}\gamma_\mu \nu\right) \tag{1.8}$$

where the G_F is the Fermi constant $G_F = 1.166\dot{1}0^{-5} GeV^{-2}$.

Nevertheless, the non-relativistic limit leads to an incomplete theory. The interaction considered with a 2-components spinor transforms a proton into a neutron without changing the position, the spin or the parity. However, T.D. Lee and C.N. Yang have postulated in 1956 that the weak interactions violate the parity after analysing the decays of the τ and θ particles[19]. The Wu experiment [26] confirmed this hypothesis in 1957 by studying the decay of ^{60}Co.

The Fermi interaction was modified by Feynman and Gell-Mann[14] to a $V - A$ theory[1]. The vector current is now subtracted by an axial vector current. For example, the neutrino current is replaced by:

$$\begin{aligned} \overline{e}(x)\gamma_\mu \nu \quad \rightarrow \quad & \overline{e}\gamma_\mu (1-\gamma_5)\nu \\ & = \overline{e}\gamma_\mu \nu - \overline{e}\gamma_\mu \gamma_5 \nu \end{aligned} \tag{1.9}$$

It was established that the weak current has the form $V - A$ instead of $V + A$. The weak interaction is only coupling left-handed particles and right-handed anti-particles.

The lagrangian describing the weak interactions can be written as a currents interaction:

$$\mathcal{L}_{weak} = -\frac{G_F}{\sqrt{2}} J^\mu J^\dagger_\mu \tag{1.10}$$

and J^μ is a combination of leptonic and hadronic currents.

Contrary to the QED, the weak interaction obeys to a non-Abelian symmetry group[2], the SU(2) symmetry group. The matter field could be represented as a doublet Ψ_L and a singlet Ψ_R of this group.

[1] V stands for vector and A for axial-vector

[2] A group is non-Abelian when the elements of the group are not commutating.

$$\Psi_L = \begin{pmatrix} \nu_{eL} \\ e_L \end{pmatrix}, \quad \Psi_R = e_R \tag{1.11}$$

The generators of the group are the three Pauli matrices σ_i, associated with a gauge field W^i_μ. The bosons of the weak interactions are the $W^\pm$ and Z.

As the left-handed leptons are combined into a doublet, a quantum number called weak isospin (I_3) is associated with them. The charged leptons have a weak isospin $I_3 = \frac{-1}{2}$ and for the neutrinos $I_3 = \frac{1}{2}$. Concerning the gauge bosons $W^\pm$ and Z, the weak isospin is respectively $I_3 = \pm 1, 0$.

Quantum Chromodynamics

The Quantum Chromodynamics (QCD) is the quantum field theory of the strong interaction. In this model, the interaction is due to an SU(3) gauge group. It produces 8 gauge fields called gluons. The spinors of this theory are the six quarks that form a triplet with respect to the gauge symmetry.

The SU(3) gauge group is a group of $9 - 1 = 8$ real parameters and of 8 generators. Those generators are the Gell-Mann matrices. The normalised generators are defined by:

$$T^a = \frac{1}{2}\lambda^a \tag{1.12}$$

The structure constant f^{abc} can be expressed as:

$$if^{abc} = 2Tr([T^a, T^b]T^c) \tag{1.13}$$

Some theories arguments and the results of experiments in high energy physics have required introducing six spinor fields, the quarks. Each of them is considered as a triplet state with respect to the SU(3) group:

$$q_i = \begin{pmatrix} q_i^1 \\ q_i^2 \\ q_i^3 \end{pmatrix} \tag{1.14}$$

where q_i are the six quarks. These quarks can appear in three different states, called color and that are named red, blue and green.

The local gauge symmetry U(1) should be included into the SU(3) group.

The gauge field A_μ can be introduced in the group:

$$A_\mu = g_S A_\mu^a \frac{\lambda^a}{2} \tag{1.15}$$

with a = 1,...,8 and corresponds to the 8 gluons. A mass term $m_g A_a^\mu A_\mu^a$ would not be gauge invariant, it implies that the gluons have to be massless.

The covariant derivative is then:

$$\begin{aligned} D_\mu &= \partial_\mu - iA_\mu \\ &= \partial_\mu - ig_S A_\mu^a \tfrac{\lambda^a}{2} \end{aligned} \tag{1.16}$$

The QED field $F_{\mu\nu}$ is not gauge invariant in QCD. Nevertheless, an additional term to obtain gauge invariant field tensor can be introduced:

$$G_{\mu\nu}^a = \left(\partial_\mu A_\nu^a - \partial_\nu A_\mu^a\right) + g_S f^{abc} A_\mu^b A_\nu^c \tag{1.17}$$

Finally, the QCD Lagrangian is given by:

$$\mathcal{L} = \sum_{i=1}^{6} \bar{q}_i \left(i\gamma^\mu D_\mu - m_i\right) q_i - \frac{1}{4} G_{\mu\nu}^a G_a^{\mu\nu} \tag{1.18}$$

1.2 The Glashow-Weinberg-Salam model

Rephrase the section title

Late 1960, a model of unification was postulated by Glashow, Weinberg, and Salam to describe the electroweak interaction (EW). The theory rests on a $SU(2)_L \otimes U(1)_Y$ symmetry group. It is the simplest group which conserves the properties of EM charge conversion and parity violation of weak interaction.

For the EW unification, the $U(1)_{EM}$ symmetry group describing the EM has to be rewritten. As the fermions are considered by left-handed doublets and right-handed singlets, the $U(1)_{EM}$ will break the gauge invariance. The weak isospin group $SU(2)_L$ is combined with the EM charge to create the hypercharge give by the Gell-Mann-Nishijima relation:

$$Q = I_3 + \frac{1}{2} Y \tag{1.19}$$

The I_3 term is the third component of the weak isospin. With the introduction of the hypercharge, the EM gauge invariance is conserved.

The EW Lagrangian could be given as:

$$\mathcal{L}_{EW} = \mathcal{L}_{YM} + \mathcal{L}_{fermions}\textbf{??} \tag{1.20}$$

The first term $\mathcal{L}_{YM}$ is the Yang-Mills Lagrangian that describes the bosons gauges interactions (kinetic term + interaction between bosons). It has the form below:

$$\mathcal{L}_{YM} = -\frac{1}{4}\mathbf{W}^a_{\mu\nu}\mathbf{W}^{a\mu\nu} - \frac{1}{4}\mathbf{B}_{\mu\nu}\mathbf{B}^{\mu\nu} \tag{1.21}$$

With

$$\mathbf{W}_{\mu\nu} = \partial_\mu \mathbf{W}_\nu - \partial_\nu \mathbf{W}_\mu - ig[\mathbf{W}_\mu, \mathbf{W}_\nu] \tag{1.22}$$

$$\mathbf{B}_{\mu\nu} = \partial_\mu \mathbf{B}_\nu - \partial_\nu \mathbf{B}_\mu \tag{1.23}$$

In the equation 1.22, $\mathbf{W}_\mu = \sum W^i_\mu \sigma^i/2$ is a vector of three gauge fields associated to $SU(2)_L$ and σ^i are the Pauli matrices. The term $[\mathbf{W}_\mu, \mathbf{W}_\nu]$ is associated to the interactions between the gauge fields. In the equation 1.23, $\mathbf{B}_\mu$ is the only gauge field associated to the $U(1)_Y$.

The Lagrangian describing the fermions field is given by:

$$\mathcal{L}_{fermions} = \overline{\Psi}_L\gamma^\mu D_\mu \Psi_L + \overline{\Psi}_R\gamma^\mu D_\mu \Psi_R \tag{1.24}$$

With $D_\mu\Psi_L = \left(\partial_\mu + ig\mathbf{W}_\mu - i\frac{g'}{2}Y\mathbf{B}_\mu\right)\Psi_L$ and $D_\mu\Psi_R = \left(\partial_\mu - i\frac{g'}{2}Y\mathbf{B}_\mu\right)\Psi_R$ (1.25)

In the equation 1.25, the covariant derivative has two forms. The weak interaction does not allow coupling of the W bosons to right-handed fermions whereas the γ and Z bosons do.

With the EW Lagrangian described above, the gauge bosons were considered as massless fields. The electroweak interaction does not allow a $m\overline{\Psi}\Psi$ term because it does not transform as a scalar under $SU(2)_L \otimes U(1)_Y$. Moreover, the $m^2\mathbf{W}_\mu\mathbf{W}^\mu$ violates the $SU(2)_L$ gauge invariance of the Lagrangian. The mass terms associated with the physical fields of the gauge bosons are given by spontaneous symmetry breaking via the Higgs mechanism.

1.2.1 Symmetry Breaking mechanism and Goldston theorem

Before to introduce the Higgs mechanism, we will study the spontaneous symmetry breaking for a global symmetry. This phenomenon is also seen in phase transitions or laser theory.

Let's consider first the Lagrangian density for a complex scalar field ϕ:

$$\mathcal{L} = \partial^\mu \phi^* \partial_\mu \phi - \mu^2 \phi^* \phi - \lambda(\phi^* \phi)^2 \tag{1.26}$$

The first component of the Lagrangian density corresponds to the kinetic term of a complex scalar field, while the second component is related to a scalar potential. The coefficient μ^2 is a real parameter. Nevertheless, depending on its sign, the potential can take two forms.

If $\mu^2 > 0$, the symmetry is unbroken and the potential has a minimum at $\phi = 0$ which does not degenerate. It describes a particle with a mass μ and a quartic self-coupling. As the transformation $\phi \to -\phi$ is respected, this solution is a symmetric one.

When $\mu^2 < 0$, there is not a unique ground state for this system but multiple states with the same vacuum energy. The minima is located on a circle of radius:

$$v = \sqrt{\frac{-\mu^2}{2\lambda}} > 0 \tag{1.27}$$

By choosing a particular solution as the ground state, the symmetry gets spontaneously broken.

A parametrisation of the excitations around the ground state is possible by introducing a new field ϕ:

$$\phi(x) = \frac{1}{\sqrt{2}}\left(v + \rho(x) + i\Theta(x)\right) \tag{1.28}$$

The value v is given by one of the solution from equation 1.32, $\rho(x)$ and $\Theta(x)$ are real fields.

By adding the new field in the equation 1.26, the Lagrangian becomes:

$$\mathcal{L} = \frac{1}{2}(\partial_\mu \rho)^2 + \frac{1}{2}(\partial_\mu \Theta)^2 - \lambda v^2 \rho^2 - \lambda v(\rho^3 + \rho\Theta^2) - \frac{\lambda}{4}(\rho^2 + \Theta^2)^2 \tag{1.29}$$

The field $\rho(x)$ describes a state of mass $m_\rho = 2\mu^2$, coupled to the massless field $\Theta(x)$.

The field $\Theta(x)$ describes excitations around a direction in the potential. The excitations are not costing any energy, so they correspond to massless bosons called Goldstone bosons.

1.2.2 Higgs mechanism

As we have seen with the Lagrangian of the QED and QCD, the bosons generated are massless. Nevertheless, the W$^\pm$ and the Z bosons have a mass and the equation **??** of the EW interaction does not include a mass generator. The origin of the fermions masses is solved in the SM thanks to the Higgs-Englert-Brout mechanism [16][12].

Lets consider first a doublet of complex scalar fields Φ:

$$\Phi = \begin{pmatrix} \phi^+ \\ \phi^0 \end{pmatrix} \tag{1.30}$$

The invariant Lagrangian density under $SU(2)_L \otimes U(1)_Y$ gauge transformation is:

$$\mathcal{L} = (D^\mu \phi)^\dagger (D_\mu \phi) - V(\phi) \tag{1.31}$$

The covariant derivative is the one of $SU(2)_L \otimes U(1)_Y$ given by the equation 1.25 and represents the kinetic term. The Higgs potential is similar to the one considered first and has also two solutions depending on the sign of μ^2. Let's focus only on the negative solution. There is an infinite set of degenerated states with minimum energy:

$$\phi_0 = \sqrt{\frac{1}{2}} \begin{pmatrix} 0 \\ v \end{pmatrix} \text{ with } \; v = \sqrt{\frac{-\mu^2}{\lambda}} > 0 \tag{1.32}$$

Let's expand the field Φ around its minima by including a field $h(x)$ which describes quantum fluctuations and three massless Goldstone fields, denoted $\theta^i(x)$:

$$\Phi(x) = e^{i \frac{\sigma_i}{2} \theta^i(x)} \frac{1}{\sqrt{2}} \begin{pmatrix} 0 \\ v + h(x) \end{pmatrix} \tag{1.33}$$

A particular gauge can be defined in a way that the Goldstone fields are absorbed by the physical field of $SU(2)_L \otimes U(1)_Y$. It implies the apparition of mass terms in equation 1.31. First, we are interesting in the mass generation mechanism, we will focus only on the impact of the new field on the derivative covariant, we will omit any h-mixed terms and drop down the partial derivative:

$$\left|\left(i\frac{g}{2}\mathbf{W}_\mu + i\frac{g'}{2}Y\mathbf{B}_\mu\right)\Phi\right|^2 = \frac{1}{8}\left|\begin{pmatrix} gW_\mu^3 + g'B_\mu & g(W_\mu^1 - iW_\mu^2) \\ g(W_\mu^1 + iW_\mu^2) & -gW_\mu^3 + g'B_\mu \end{pmatrix}\begin{pmatrix} 0 \\ v \end{pmatrix}\right|^2 \tag{1.34}$$

The charged fields can be expressed as a linear combination of gauge field:

$$W_\mu^\pm = \frac{W_\mu^1 \mp iW_\mu^2}{\sqrt{2}} \tag{1.35}$$

The eigenstates are rewritten as decorrelated terms representing the neutral fields from the EW symmetry group:

$$Z_\mu = \cos\theta_w W_\mu^3 - \sin\theta_w B_\mu \tag{1.36}$$

$$A_\mu = \sin\theta_w W_\mu^3 + \cos\theta_w B_\mu \tag{1.37}$$

θ_w is the Weinberg angle and represent a bound between the coupling g and g':

$$\sin\theta_w = \frac{g'}{\sqrt{g^2 + g'^2}} \ \textit{and} \ \cos\theta_w = \frac{g}{\sqrt{g^2 + g'^2}} \tag{1.38}$$

The equation 1.34 becomes:

$$\begin{aligned} \left|\left(i\tfrac{g}{2}\mathbf{W}_\mu + i\tfrac{g'}{2}Y\mathbf{B}_\mu\right)\Phi\right|^2 &= \tfrac{1}{8}\left|\begin{pmatrix} A_\mu\sqrt{g^2 + g'^2} & gW_\mu^- \\ gW_\mu^+ & -Z_\mu\sqrt{g^2 + g'^2} \end{pmatrix}\right|^2 \\ &= \tfrac{1}{2}M_Z^2 ZZ^* + \tfrac{1}{2}M_W^2 W^- W^+ \end{aligned} \tag{1.39}$$

With $M_Z = \frac{1}{2}v\sqrt{g^2 + g'^2}$ and $M_W = \frac{1}{2}vg$, the mass of the Z boson and the $W^\pm$ bosons. The mass of the photon is coherent to the expectation and is null.

The Higgs mechanism implies the existence of a massive gauge field, the Higgs boson. It is coupled to the other bosons and also to itself. This could be shown by extending the Higgs potential with the field defined in equation 1.33:

$$-\lambda v^2 h^2 - \lambda v h^3 - \frac{1}{4}\lambda h^4 \tag{1.40}$$

The first term gives the mass of the Higgs boson, $M_H^2 = 2\lambda v^2$, while the second and third terms are the Higgs self-interactions. The Higgs mass can not be predicted by the theory because it is given by a function of the parameter λ, which is one of the free parameters of the SM.

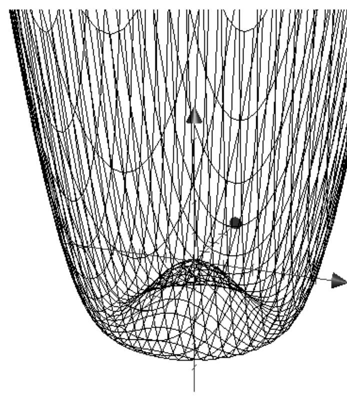

Figure 1.2 – Scalar potential: ADD A GOOD CAPTION.

Yukawa couplings with fermions

1.3 Beyond the Standard Model

The SM constitutes one of the most successful achievements in modern physics. One of its strength is to provide an elegant theoretical framework to describe the known experimental facts about particles, but also it was able to predict the existence of a mechanism to generate the particle masses via the Higgs mechanism. Nevertheless, a lot of mysteries in the Universe are not explained by this theory.

1.3.1 Limitations of the Standard Model

Despite the fact that the experimental results are not contradictory to the SM, the theory is far away to be the answer to all the questions. The particle physics community is facing a challenge to find the ultimate theory of everything. An exhaustive list of some limitations is going to be presented.

Free parameters

The SM does not explain the existence of the free parameters, which are to the number of 19. It does not explain also why there are three generations of particles and why the gap between generations is spread over five orders of magnitude.

This is not really a problem for the physics itself, nevertheless, the particles physics community has a lack of understanding these values.

Hierarchy problem

The hierarchy problem refers to two main scales problem about the SM.

First of all, the difference between the energy scale of the SM and the Planck scale is of the seventeen orders of magnitude. No "intermediate" physics have been found between the two scale.

A second problem occurs while considering the Higgs boson mass. The SM does not predict its mass, but it sets some theoretical bounds with respect to Λ, the scaled energy at which the SM is not valid anymore. The theoretical Higgs mass is higher that what it should be compared to the EW scale. The Higgs interacts with the particles of the SM (fermions, W and Z boson), but it also interacts with himself. Due to the scalar nature of the boson, they are quartic divergences while calculating the loop corrections. The quantum corrections, which take into account the coupling of the Higgs, are Λ^2 divergent and lead to a huge Higgs mass. To avoid that, delicate cancellations should occur between the quantum corrections. These cancellations are known as the fine-tuning problem.

Gravitation

Although particles physicists are dreaming of a "theory of everything" that will unify the electroweak, strong and gravitational interactions, there is no viable theory to describe the gravity in a quantum point of view to include it in the SM and which would be still valid at a macro-scale.

Neutrino mass

The neutrinos defined by the SM are assumed to be exactly massless. Nevertheless at the end of the 90's, the Super Kamiokande experiment had surprising results. There was a lack on the expected solar and atmosphere neutrinos flux. The result was interpreted by an oscillation of neutrinos between the three leptonic flavors. However, the oscillation is possible only if the neutrino has a mass. That phenomenon could be considered as a proof of physics beyond the SM.

Matter-antimatter asymmetry

As discussed at the beginning of this chapter, the SM defines an equal number of particles and anti-particles. Although everyone assumes that the matter and antimatter were created in an exactly equal amount by the Big Bang, a mechanism has favoured electrons, protons, and neutrons to positrons antiprotons and antineutrons. If the amount of matter and antimatter was equal, our Universe would have been completely annihilated. The matter domination could be a local phenomenon with an antimatter surrounding the region. However, the region of contact between matter and antimatter would be a violent place of interaction, which would disturb the cosmic microwave background.

An assumption to explain the asymmetry is that the antimatter was produced in an infinity proportion compared to the matter. Hence, the annihilation as lead to create a Universe only made of matter. A mechanism which tends to prefer the matter has been observed in the study of the kaon oscillation. This particle is able to transform spontaneously to its own antiparticle and vice-versa. Nevertheless, this transformation is not symmetric: the kaon is slower to turn into an antikaon than the inverse transformation. Unfortunately, the SM provides no explanation about that mechanism.

Dark Matter

Several astrophysical observations are indicating that the Universe is made not only of visible matter but also of matter that seems to be invisible to the electromagnetic interaction, the dark matter. In 1933, a measurement of the galaxies velocities in the Coma cluster to determine the cluster mass gives a surprising result. The mass was more than two orders of magnitude bigger than the mass of visible stars in the cluster. It was found that the matter of the SM describes only 5% of the Universe content. The rest of the Universe is made of 22% of dark matter and around 73% of dark energy. The neutrinos are possible candidates to dark matter, as it couples to SM matter via only weak interaction, but they cannot account for the entire density of the universe. Nowadays only twelve particles (plus the anti-particles associated) have been observed. The idea of dark matter comes from the way we the mass of a galaxy is estimated.

1.3.2 Theories beyond the Standard Model

Supersymmetry

The Supersymmetry (SUSY) is a QFT, that relates the elementary fermions known to corresponding bosons, called sfermions and the bosons to corresponding fermions, sbosons [25]. The related particles are called super-partners. They have the same mass, the same quantum numbers but the spin is differing by a half factor. SUSY might be a broken symmetry. This will allow the super-particles to acquire very high masses.

SUSY is a good candidate for physics beyond the SM. It will solve the hierarchy problem without any fine tuning. For example, the loop contributions of one particle to the Higgs are cancelled by the loop contributions of its super-partner. It will be able to provide a framework for the unification of the three gauge interactions at a GUT scale. The lightest super-particle is a good candidate for the Dark Matter.

Despite it will answer many questions from the SM, there is a lack of understanding why SUSY is a broken symmetry.

Grand unification theory

After the success of the electroweak unification, the next step is to include the strong interaction to build the Grand Unification Theory (GUT), an extension of the SM. In this framework, the three forces are different manifestations of a single interaction. It includes the $SU(3)_C \otimes SU(2)_L \otimes U(1)_Y$ symmetry group into a larger $SU(5)$ group. The quarks and leptons are ordered in left decuplets and right quintets. The coupling constants are described by only one parameter. There are 24 mediators, the 12 mediators of the SM plus 6 X mediators (charge $\pm 4/3$ and 3 colors) and 6 Y mediators (charge $\pm 1/3$ and 3 colors). It predicts the existence of new particles as leptoquarks[3], multiple Higgs bosons and new currents.

Unfortunately, the theory is not validated because of its prediction of the proton lifetime. The first GUT was introduced by Georgi and Glashow in 1974 and was predicting a decay of the proton. The actual experimental limit of the proton lifetime is set to 5×10^{32} years, whereas the predicted lifetime defined by the SU(5) group is one order of magnitude lower. [24]

Technicolor

The technicolor is a theory that explains the mass generation. Contrary to the EW symmetry, the masses of particles are not generated by the spontaneous symmetry breaking but they are generated by a strong gauge interaction. This interaction is strong and confined at the energy that has been experimentally probed. The approach of the theory avoids the hierarchy problem induced by the SM.

String theory

The particle physicists have the dream of unifying the forces of the nature to have only one single interaction with four different manifestations. The string theory proposes a framework for the "theory of everything". The basic unit of matter is no more considered as particles but a one-dimensional string of which particles are various vibrational modes.

The string theory is a theory of quantum gravity. It tries to unify the gravitation to the quantum Extra dimensions of 10 -11 space-time dimensions. Possible explanation for the hierarchy problem.

1.4 Conclusions

We have seen the beauty and the limits of the SM. The high energy physics community is trying to study as far as possible the limit of the SM and is also trying to find some proof of new physics beyond the SM. The (LHC) at CERN has permitted in 2012 to point out the existence of a Higgs boson. Nevertheless, the beam structure of the LHC is not efficient enough to

[3] Coupling between a lepton and a quark

perform very precise measurements. Because of the collision between protons, the energy of the collision can't be exactly known. The next chapter deals with a future experiment in high energy physics, where electrons and positrons are used to probe the matter instead of protons and antiprotons.

Chapter 2

The future of high-energy physics: the International Linear Collider

Since 2008, the Large Hadron Collider (LHC) is actually the most powerful tool in high-energy physics to have a better understanding of the universe, particularly with the discovery in 2012 of a new particle compatible to the boson predicted by the spontaneous symmetry breaking of the SM [1, 9]. Although the LHC is an impressive machine able to reach the highest energy scale of collision available on Earth with a centre-of-mass energy of 13 TeV, the complex environment of the events generated hides the access to some fundamental parameters. To achieve more precise measurements of the Higgs boson, but also to test the validity of the SM and other physics theories introduced in the chapter 1, the high energy physics community has merged on the necessity to build a linear electron-positron collider, that will work as a complementary accelerator to the LHC.

This chapter will explain the motivations to invest a huge amount of money in a new great world project. It will present the complementary nature of the lepton and hadron colliders and the main advantages of the lepton collisions will be discussed. After giving an overview of the ILC with its basic design and the experiment models, we will focus on the design of one of the detectors: the International Large Detector (ILD).

Contents

2.1 To a linear lepton collider

The most impressive accelerator ever built is located at CERN in Geneva, Switzerland. It is the world largest particle accelerator, with a circumference ring of nearly 27 kilometers, straddling the Swiss and French borders. It is designed to collide two counter rotating beams of protons or heavy ions, with a possibility to reach centre-of-mass energies of 13 TeV with a high peak luminosity of 10^{34} cm^{2}s^{-1}. The goals of the LHC are to perform further tests on the SM, search for new forces or produce dark matter candidates. Indeed, the collider covers a wide energy range at the constituent level while running at a fixed beam energy. Unfortunately, due to the nature of the particles used, the experiment can not reach the highest precision measurements needed.

Complementary to a discovery machine such as the LHC, a machine to perform precise measurement should be built: the linear lepton collider.

2.1.1 Advantages of a linear lepton collider

First of all, during each collision at an hadron collider, only a part of the total centre-of-mass energy is available for the process evolved, therefore the initial four-vector momentum is not known. By colliding leptons, which are structureless objects, the full centre-of-mass energy is available for the elementary process. The initial four-vector momentum of an interaction is exactly known, hence the event can be fully reconstructed.

Secondly, with a lepton collider, the beam energy is tunable and both electron and positron beams can be polarised. The selection of an appropriate polarisation can boost the signal and suppress the background cross-section.

Thirdly, as seen in the first point, at the LHC, only a fraction of the partons are contributing to the interesting process. The proton-proton interaction cross section is dominated by inelastic background QCD processes. The signal event is then accompanied by large backgrounds produced by the interaction of other parton collisions. This background masks the elementary process of interests, in order that it has an impact on the detector design, that should have a high radiation tolerance and implement a selective trigger to reduce the data rate. The lepton colliders do not suffer from this kind of background and at similar energies, the event rate is lower as those of hadron colliders. Moreover, the interaction of electrons and positrons is purely electroweak. In consequence, the detector does not have to handle extreme data rates and can be used without any trigger. Hence, the sensitivity to any possible signature of new physics is improved.

Although the leptons, in particularly the electron and positron, have clearer advantages on hadrons to perform a precise measurement, the choice of a linear collider comes from the physics of accelerating charged particles. While charged particles are moving in a circular accelerator, they lose some energy by emitting photons via synchrotron radiation. The equation 2.1 describe the energy loss via synchrotron radiation:

$$\Delta E_{sync} \sim \frac{E^4}{m^4 r} \tag{2.1}$$

The radiative energy loss is proportional to the radius r of the accelerator, the energy of the particle E to the power of the fourth and its mass m to the power of the fourth. As the electron mass is $\sim 1.8 \times 10^3$ smaller than the proton mass, the energy loss radiated by the electron is bigger than the energy loss radiated by proton at the same centre-of-mass energy. To compensate the energy loss, a circular electron-positron accelerator should have an extremely big radius (bigger than the actual LHC), increasing the cost to build the experiment. Another solution to overcome the synchrotron radiation is to accelerate the particles in a linear collider. Nevertheless, the centre-of-mass energy has to be reached in only one path, whereas the bunch of particles in a circular collider is accelerated many times in the ring until the desired energy of collision is reached. To still get an "affordable" experiment, the centre-of-mass energy obtained at a linear collider is below to the one from a circular collider. Indeed, to work at the same energy scale, a linear collider would require a bigger number of accelerating cavities and would make a much bigger and more expensive collider than a circular one.

2.1.2 Future linear lepton collider

As it was mentioned before, the precise measurements offered by lepton collider is one of the key points to constrain the limits of the SM and to characterise precisely all the known particles. Since the 1980's, several linear collider technologies have been developed, leading in the 1990's to five major accelerator technologies: Superconducting Radio-Frequency (SRF), the Compact LInear Collider (CLIC) technology and three different normal conducting technologies (S-band, C-band, and X-band)[10]. At the beginning of the 2000's, a committee for the future linear collider was formed and has chosen in 2004 the SRF technology[17] and since then all the efforts are done in that direction to build the International Linear Collider (ILC). The technology developed for this future experiment is also used for the XFEL at DESY in Hamburg and at KEK in Japan. Another linear collider project led by the CERN is being prepared: the CLIC. It has a more challenging technology to aim a nominal energy of 3 TeV instead of 1 TeV for the ILC. Contrary to the ILC, CLIC plans to use radio-frequency structures and a two beam concept. Another idea would be to develop a muon collider instead of electron-positron collider[21]. As the electron, the muon is a pointlike particle, therefore the centre-of-mass energy can be easily adjusted to perform a precise study. The muon mass is 207 times much bigger than the electron ones and suffers less of energy loss by synchrotron radiation. Hence, a circular collider could be more adapted and the beamstrahlung effects would be smaller in a muon collider than in an e^+e^- machine. Nevertheless, the muon has a lifetime of only 2.2 μs making up a more challenging acceleration design.

Paper on ILC

Paper on CLIC

For the purpose of this thesis, the CLIC and muon colliders will not be described more to focus on details on the ILC.

2.2 The ILC machine

The ILC should be the next lepton collider experiment and will be situated in Japan. During 2016, the physicists community is waiting for an official decision of the Japan government concerning final site where the experiment will be held. At the time this thesis was written, the most likely site candidate is located in the north of Japan, in the region of Kitakami.

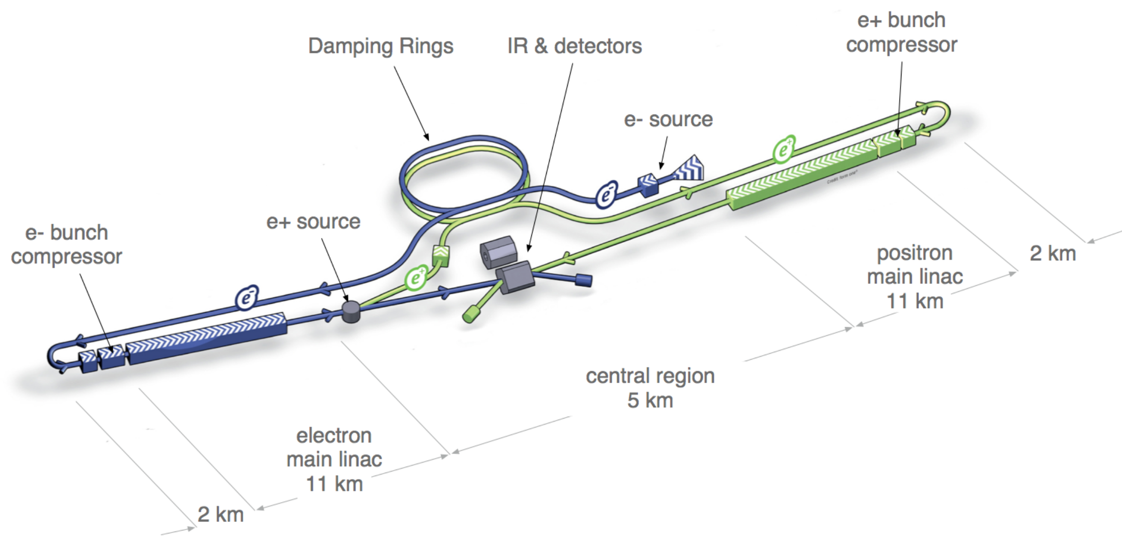

Figure 2.1 – Schematic layout of the International Linear Collider (ILC).[6]

2.2.1 Baseline design

The ILC is planned to collide electrons and positrons at a center-of-mass energy up to 500 GeV, with an energy variability down to 200 GeV for 31 kilometers long accelerator. An upgrade to reach the centre-of-mass energy of 1 TeV is also possible, but the accelerator should be extended to achieve a total length of 50 kilometers. It is designed to generate a total of 500 fb^{-1} of data during the first four years of operation. The luminosity will reach a peak of $2 \times 10^{34}\mathrm{cm}^{-2}\mathrm{s}^{-1}$ at $\sqrt{s} = 500$ GeV.

The main components of the ILC are presented in the following order: first of all, an overview of the electron source and their acceleration via the conducting and superconducting structures, then the role of the damping rings, the injection into the main linacs, followed by the positron source and the Beam Delivery System (BDS) to finally present the interaction region (IR). A detailed description of the ILC could be found in the Technical Design Report[2].

2.2.2 Machine design and beam parameters

The polarised electrons are produced by a laser firing a strained GaAs photocathode in a Direct-current (DC) gun. To implement a redundancy, the electron generation system is made of two lasers and DC guns, providing bunches with a polarisation of 90 %. The electrons are then pre-accelerate to 76 MeV thanks to non-superconducting accelerating structures. Thereafter, they are injected into a 250 m long superconducting linac to reach the energy of 5 GeV. Nevertheless, the dimension and density of bunches are quite extended, thus their emittance is too wide. Before to inject the bunches into a damping ring, which is used in order to decrease the emittance and reach the desired luminosity, superconducting solenoids rotate the spin vector into the vertical direction, while SRF cryomodules are used for an energy compression.

The damping ring is 6.7 km length and made of magnets and wrigglers that are going to force the particles to get a bent track. This system is used to dump the electrons with large transverse and longitudinal emittance to the low emittance required for the luminosity production. The reduction of the emittance should be achieved within 200 ms between the machine pulses. Although the positron source was not yet introduced, their bunches suffer from the same problems as the electron ones. A second damping ring, placed in the same cavern as the electron one, is also in charge to get the desired emittance.

The bunches are then extracted from the damping rings and transferred via the Ring To the Main Linac (RTML) structure, the longest continuous beam line at the ILC. It is divided into five subsystems to transport the bunches from the damping rings to the BDS, in order to orient the beam in the desired polarisation by rotating the spin of the particle, but also to compress the beam bunch length from several millimeters to a few hundred microns thanks to a two-stage bunch compressor. At the same time the bunches are compressed, sections of SRF technology accelerate the bunches from 5 GeV up to 15 GeV. One of the challenges of the RTML is to preserve the emittance obtained after the damping rings, while the length and the energy of the bunches are tunned. Then, the particles are delivered to the main Linac, an 11 km long accelerator using 1.3 GHz SRF cavities, made of niobium.

Before to reach the interaction region, the primary electron beam is transported through a 147 m superconducting helical undulator to produce photons from $\sim$ 10 up to $\sim$ 30 MeV, depending on the energy of the primary beam. This primary beam is separated from the photons and sent back to the BDS with an energy loss of $\sim$ 3 GeV. The photons are directed onto a rotating Ti-alloy target to create e^+e^- pairs that are separated. The positrons collected are accelerated to 125 MeV thanks to a normal conducting linac and then accelerated to 5 GeV with a superconducting boost linac. Finally, they are introduced into the damping ring to reduce their emittance.

The two beams are transported from the high energy LINACS to the IR by the BDS, in charge to focus the beams to the sizes required to meet the ILC luminosity wanted. It is divided into five main subsystems. First, in the direction of the beam, a system is in charge to perform some emittance measurement and matching, to give a trajectory feedback, and provide a polarimetry and energy diagnostic. Then the beam is collimated to remove the beam-halo particles that would generate a huge amount of background in the detector. Muons generated during the collimation process are deflected by magnetised iron shielding. Thereafter, strong compact quadrupoles focus the beam to the sizes required to meet the desired luminosity. Before the collisions, crab cavities rotate the bunches in the horizontal plane for effective collisions and to achieve a 14 mrad total crossing angle. After the collisions, an extraction line is dedicated to transport the beams into the main beam dump.

Although two experiments will run at the ILC, there will be only one interaction region due to cost reasons. Indeed, to have two experiments running at the same time, it requires two separate BDS of 4 km long each. Thanks to a push-pull scheme, the detectors will work alternatively: while one is taking data, the other one is sitting in the garage to be maintained. The two detectors will be presented in more details at section 2.3.

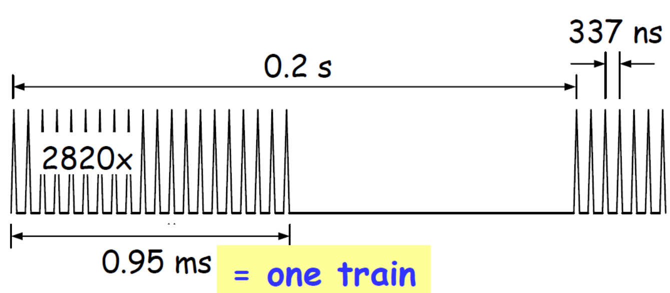

Figure 2.2 – Representation of the bunch structure at the ILC. One bunch train is made of 2625 bunch crossings and lasts 0.95 ms. Each bunch crossing is spaced out by 337 ns. Two bunch trains are of 0.2s apart from each other.[20]

Draw my one bunch structure figure...

The accelerator described above will create bunch trains at a repetition rate of 5 Hz. Each train is composed of 2625 bunches that contain 2×10^{10} particles and lasts 0.95 ms. The interval between two trains is 2 ms long.

This structure is a feature key to develop detectors able to be switched off during the dead time in order to reduce the power consumption.

2.2.3 Beam backgrounds

To design the detectors of the ILC, the backgrounds must be understood and taken into account to give optimal performances. Tthe event reconstruction becomes more complicated with hits caused by background particles. They are two kinds of background, the one created by the BDS and the one related to the interaction point. As it was discussed in the subsection 2.2.2, the collimator placed closed to the interaction point (IP) to purify the beam can produce muons by an electromagnetic shower. To sweep them away, iron spoilers are used to create a magnetic field and deflect the muons. A side effect is to increase the number of neutrons created in photo-nuclear reactions. A concrete wall placed at the entrance of the experimental hall vanishes the neutron background.

Contrary to the LHC, the ILC will not suffer from the QCD background, as mentioned in subsection 2.1.1 Nevertheless, due to the nature of electrons and positrons, the two beams will interact each other before they collide. The electromagnetic beam field of each bunch is high and causes the focusing of the opposite bunch. It is bending the electron/positron trajectories near the IP. On the one hand, this effect helps to focus the incoming beams and enhance the luminosity. On the other hand, as the charged particles have bending track, they are emitting hard photons via beamstrahlung, creating e^+e^- pairs background. The hard photon is strongly focused in the forward region and do not contribute strongly to the background in the detector. However, the e^+e^- pairs created contribute to the background directly or through backscattered particles. In consequence of the beamstrahlung, the beam particle energy is reduced, hence the collisions occur at different energies from the nominal one and this affects the physics cross-section. The beamstrahlung photons can also produce neutrons by hitting components. The other source of hard photons is the initial state radiation. With the beamstrahlung, they contribute reducing the luminosity[22].

Different kinds of soft pairs background can be expected at the ILC: the coherent and incoherent pair production. The coherent pair production appears when beamstrahlung photons are interacting with the strong electromagnetic field of the beams. In the ILC environment the coherent pair background are negligible, whereas the incoherent pair production is dominant. It corresponds to e^+e^- pairs created by the interaction of only two particles. They are to the number of three depending on the nature of the scattered photons creating the e^+e^- pair. The Bethe-Heitler process corresponds to the scattering of one real photon while the second one is virtual. It contributes to approximately two of the third pair production. The second process is the Landau-Lifshitz, where the two scattered photons are virtuals and contribute to approximately to the third of the pair creation. The last production occurred via two real photons (Breit-Wheeler process) and contribute only to a percent level. The incoherent e^+e^- pairs are produced at a relatively low transverse momentum and are emitted in the forward direction.

2.3 The ILC detectors concept

2.3.1 Overview of the two experiments

As it was presented in the subsection 2.2.2, the ILC will be built with only one interaction region due to cost reasons, whereas two detectors are expected. The push-pull operation scheme will allow for data taking of one detector, while the second one is out of the beam in a close-by cavern for maintenance. The interval to switch the detectors should be short enough and of the order of one day. This time efficient implementation sets specific requirements for the beam structure but also for the detector design. The detectors should be placed on platforms to preserve the alignment and to distribute the load equally onto the floor. Another requirement on the detector design is that the magnetic fields outside the iron return yokes must be small enough to not disturb the second detector on the parking position. It is assumed that a limit of 5 mT at a lateral distance from the beam line should be sufficient.

The motivation to build two detectors with a different approach is mainly to provide a cross-checking and a confirmation of results and complementary strengths. Both detectors are optimised to study a broad range of precision measurements and search of new physics drove by the ILC expectations. Their performances are driven by the Particle Flow Algorithm (PFA) to be able to measure the final states of events with a high accuracy. To do so, both detectors should have a high hermeticity, high granularity calorimeters and excellent tracking and vertexing. The PFA is shortly presented on subsection 2.3.2.

The Silicon Detector (SiD) is a compact detector made of a silicon tracking and 5 T magnetic field. The tracking system should provide robust performance thanks to the time-stamping on single bunch crossings. The calorimeters should be highly granular to perform the PFA.

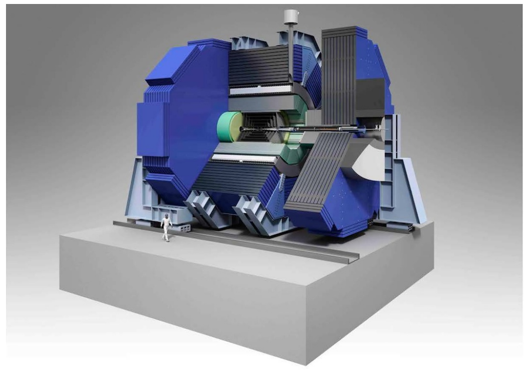

(a) The Silicon Detector

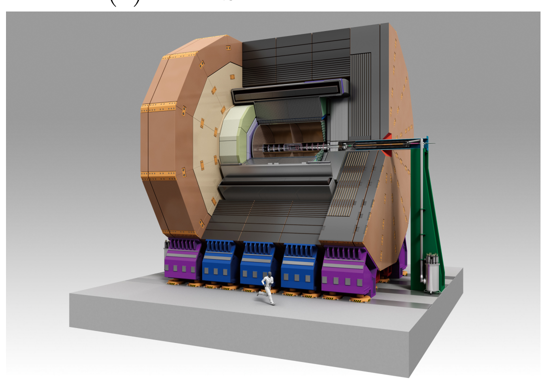

(b) The International Large Detector

Figure 2.3 – Overview of the two detectors designs at the ILC. The figure a represents the SiD design while the figure b shows the ILD approach.[7]

The second detector is the ILD. In contrast to the SiD, the tracking system is based on a continuous readout Time-Projection-Chamber (TPC) surrounded by silicon tracking detectors. The magnetic field will be only of 3.5 T combined with granular calorimeters for a good particle-flow reconstruction

2.3.2 Particle flow algorithm

The main purpose of the ILC (or the CLIC) is to achieve precise measurements of physics processes that produce final states with multiple jets. The jet energy resolution at the ILC should be sufficient to cleanly separate W and Z hadronic decays. Typically, the jet energy resolution is deduced from the equation 2.2, where α is the stochastic term usually greater than $\sim 60\%/\sqrt{E(GeV)}$.

$$\frac{\sigma_E}{E} \simeq \frac{\alpha}{\sqrt{E(GeV)}} \oplus \beta \tag{2.2}$$

The PFA approach is the extended version of the Energy Flow approach (used at H1, D0, CMS) for a highly granular detector. The goal of this framework is to achieve a stochastic term for the energy resolution greater than $30\%/\sqrt{E(GeV)}$, not reachable with a traditional calorimeter. Each sub-detector should be efficient enough to separate and to reconstruct the four-vectors of all visible particles in an event. The energy of charged particle is measured in the tracking detectors, while the energy measurements for photons are done in the electromagnetic calorimeter and neutral hadrons are done in the hadron calorimeter.

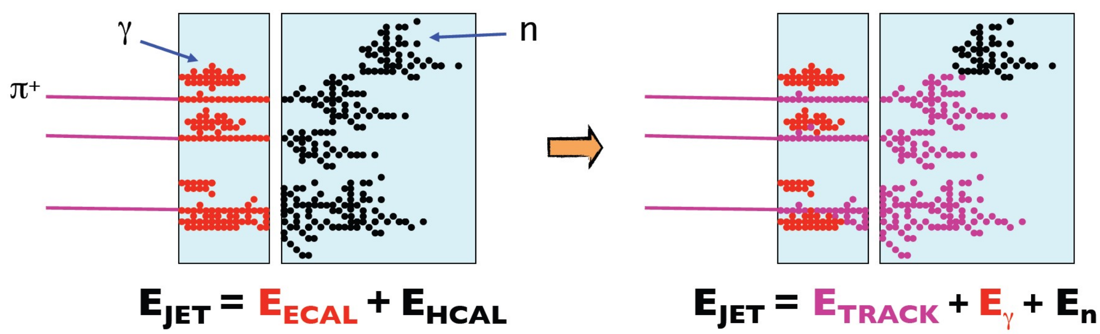

Figure 2.4 – Two different approaches for calorimetry. On the left is the traditional calorimetry method used on most of the experiments, the right one is the particle flow approach for calorimetry. The particle track is taken into account to calculate the jet energy.[15]

The PFA requirements drive the design of the detectors at the ILC. For both experiments, the electromagnetic and hadronic calorimeter have to be located inside the solenoid. Moreover, each sub-detector must be able to distinguish single particle signals, imposing a better tracking precision and higher granular calorimeters than the traditional detectors in high energy physics.

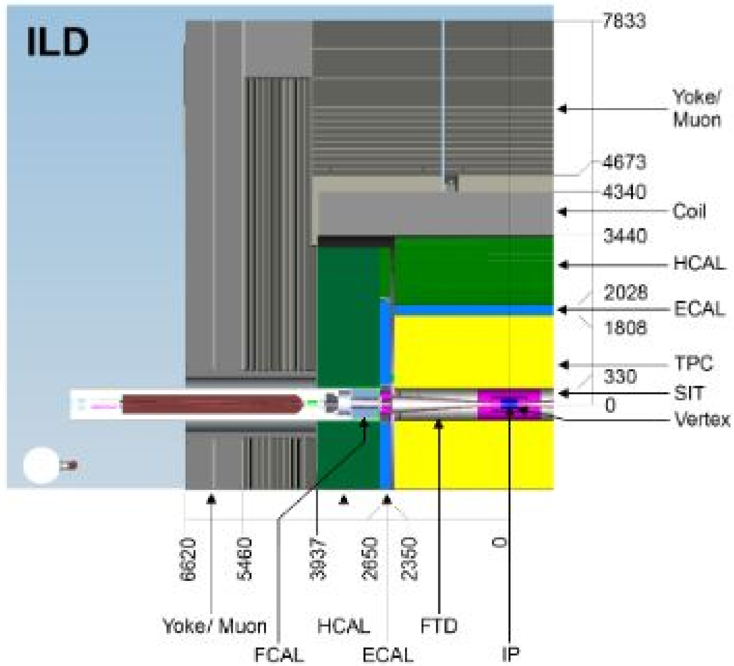

Figure 2.5 – Quadrant view of the ILD detector concept with its subdetector system [7]

2.3.3 The ILD detector

The design of ILD follows the requirements for optimal PFA performance. In summary, the detector should be highly granular to have a robust three-dimensional imaging capability. It will combine a high-precision Vertex Detector (VXD) system, a hybrid tracking system and calorimeters inside a 3.5 T solenoid. On the outside, a coil and iron return yoke will be instrumented as a muon system and a tail catcher.

Vertex detector

The chapter 4 will introduce in more details the vertex detector requirements for the ILD (material budget and precision of measurements) and the different design proposals. For the moment, two designs are under study for the vertex detector, but both of them has a pure geometry barrel. The first one is made of five single sided layers and the other one three double-sided detection layers.

Tracking

The main tracking system for the ILD is performed by the TPC. It is a gaseous detector with a low material budget designed to measure the particles' trajectory. When a particle traverses through the TPC, it ionises the gas, creating electrons that are drifting to the anode thanks to a high voltage. The anode is the part where the readout plates are installed. It provides a 3D position of the particles tracks thanks to the wires and the anode (give x-y) and the z coordinate is given by the drifting time. In addition to the exact position measurement, this detector is also able to measure the energy $\frac{dE}{dx}$ deposited by the particle and would be the first step for a particle identification.

The requirements to design a TPC at the ILC are given by two main values:

- The single point resolution $\sigma_{s.p.}$ which should be lower than 100 μm in the $r\phi$ direction and less than 500 μm in the z direction;
- The minimum distance to separate two hits which should be lower than 2 mm.

The TPC thought for the ILD is constituted of a central barrel part, with an inner radius of $\simeq$ 33 cm and a outer radius of $\simeq$ 180 cm and two endcaps with a detection area of 10 m^2. The solid angle coverage is up to $|\cos\theta \simeq 0.98|$. The barrel will be filled with a gas mixture called T2K (3 % of Ar-CF4 and 2 % of isobutane). Due to the low material budget and the ability to cope with a high magnetic field, the TPC is compliant with the PFA 2.3.2.

To improve the track reconstruction, the TPC is surrounded by high silicon detectors: two barrel components, the Silicon Internal Tracker (SIT) and the Silicon External Tracking (SET); an end-cap component, the Endcap Tracking Detector (ETD) and the Forward Tracking Detector (FTD). The SIT is linking the tracking between the VXD and the TPC, whereas the SET is giving an entry point to the Electromagnetic CALorimeter (ECAL) after the TPC. Both systems provide precise space points and improve the overall momentum resolution. The goal of the SIT is to improve the momentum resolution, the reconstruction of low p_T charged particles and the reconstruction of long-lived particles. The coupling of the SIT and SET provide also a time-stamping information.

The ETD is located within the gap separating the TPC and the endcap calorimeter. It improves the momentum resolution for charged tracks with a reduced path in the TPC. It also reduces the effect of the material of the TPC end-plate. The material budget of this end-plate is estimated to 15 % of X_0.

As the TPC does not provide any coverage in the forward region, seven silicon disks ensure efficient and precise tracking down to very small angles, whereas the ETD and the FTD make sure to get a full tracking hermeticity.

To simplify the system layout and the maintenance, the SIT, SET and ETD are made of single-sided strip layers tilted by a small angle with respect to each other. They are placed in a so-called false double-sided layers. The SIT has two layers of microstrip, instead of one layer for the SET. The technology studied are microstrip sensors with an area of 10x10 cm^2, with a pitch of 50 μm, a thickness of 200 μm and an edgeless. The dead area of the sensors will be reduced down to few microns instead of 100 μm. The spatial point resolution aimed for this detectors is $\sim$ 7.0 μm in the $r\phi$ direction. The table 2.1 gives the single point resolution aimed, as well as the angular coverage and the material budget.

Detector	Single point resolution (μm)	coverage	material budget X_0 (%)
SIT	$\sigma_{R-\phi} = 7.0$ $\sigma_Z = 50.0$	$\cos\theta \sim 0.91$	0.65
SET	$\sigma_R = 7.0$	$\cos\theta \sim 0.79$	0.65
ETD	$\sigma_X = 7.0$	$\cos\theta \sim 0.799 - 0.985$	0.65

Table 2.1 – Parameters aimed for the silicon tracker using micro-strips sensors.

The FTD is placed in the forward direction, between the beam pipe and the inner field cage of the TPC, where the magnetic field becomes less and less useful to bend charged tracks and so the determination of a precise momentum is more difficult. It consists of seven tracking disks: the two firsts are pixel detectors to cope with expected high occupancies and the five others are strip detectors. The pointing resolution will vary between $3.0 - 6.0$ μm for the two firsts layers and 7.0 μm for the five other ones.

Check the table and values....

Calorimeters

The calorimeters design is driven by the particle flow requirements. Each particle must be reconstructed individually in the detector with a jet energy measurement equal to:

$$\frac{\Delta E}{E} = 30\%/\sqrt{\frac{E}{GeV}} \tag{2.3}$$

The energy resolution obtained in equation 2.3 is obtained thanks to a combination of information from the tracking system and the calorimeters. The choice of technology used for the calorimeter will be determined by the pattern recognition performance. One of the ILD detector's goal is, for example, to be able to get a jet energy resolution sufficient to clean separate W and Z hadronic decays.

The average jet energy distribution is roughly:

- 62% of charged particles (mainly hadrons)
- 27% of γ
- 10% of long-lived neutral hadrons
- 1.5% of ν

The ECAL is the first calorimeter right after the tracking system. Its role is to identify photons and leptons and measure their energy, nevertheless, it is also the first section to develop the hadron showers. The fine segmentation makes an important contribution to hadron-hadron jet separation. For the ILD, a compromise between the performance and the cost has led to use a sampling calorimeter realised with tungsten absorber. They are three options under study for the active area. The first one called SiW-ECAL, is made of silicon pin diodes with a pitch of $5 \times 5\text{mm}^2$. It has the advantage to cover a large area, to be reliable and simple to operate, to have thin readout layers and can be operated in 3.5 T magnetic field. The second option is made of scintillator strips readout by photo-sensors and is called ScECAL. It has an active area of $5 \times 45\text{mm}^2$ arranged in alternative directions to achieve an effective granularity of $5 \times 5\text{mm}^2$ The weakness of this technology happened in dense jets environment, where the reconstruction becomes more and more complicated. Some alternatives are also thought, like the Micromegas chambers. Nevertheless, this technology is less advanced compared to the others. One other good candidate could be the use of Monolithic Active Pixel Sensor (MAPS) sensors. They have the advantage to get the signal sensing and processing on the same substrate and by choosing standard CMOS processes, the cost of fabrication would be reduced.

The HAdronic CALanalogue HCALorimeter (HCAL) has the role to separate the deposits energy of charged and neutral hadrons and to precisely measure the energy deposited. It is also a sampling calorimeter using stainless steel instead of tungsten as an absorber. The rigidity of stainless steel makes possible to get a self-supporting structure limiting the dead areas. Two baseline technologies for the active medium area are studied. The Analogue HCAL (AHCAL) is made of scintillator tiles, whereas the semi-digital, called Glass Resistive Plate Chamber (GRPC), is based on the Semi-Digital HCAL (SDHCAL).

In order to monitor the luminosity and the beamstrahlung, the calorimeter system is completed in the very forward region by three different subsystems covering very small angles also for neutral hadrons: the LumiCal, the BeamCAL, and the Low angle Hadron CALorimeter (LHCAL). The LumiCAL is placed in a circular hole of the end-cap ECAL and covers polar angles between 31 and 77 mrad. It serves as luminosity monitor by measuring the Bhabha scattering $e^+e^- \rightarrow e^+e^-$ via emission of virtual γ. Indeed, the luminosity $\mathcal{L}$ is determined by measuring the ratio of the number of counted events N_B in a considered polar angle ranged and the integral of the differential cross-section σ_B in the same region. The measurement precision should be better than 10^{-3} at 500 GeV. After each bunch crossing, the beamstrahlung pairs hit the BeamCal. This would permit to get an estimation of the bunch-by-bunch luminosity, but also to determine the beam parameters. It is placed in front of the final focus quadrupole and covers polar angles between 5 and 40 mrad. The third system, the LHCAL, ensure the coverage of the hadron calorimeter to small polar angles.

Magnetic Field and yoke

By applying a high magnetic field inside the detector, the charged particles have a bent track helping in the identification and the energy measurement. At the ILD, the nominal magnetic field is 3.5 T and should have a high homogeneity inside the TPC. Moreover, as mentioned in subsection 2.2.2, the magnetic beyond the coil has to be reduced to avoid any perturbations with the second detector in its parking position. A superconducting coil surrounding the tracking and calorimetric system generate the magnetic field. It has a diameter of 6.88 m, a length of 7.35 m and made of three modules.

Surrounding the coil, an iron yoke ensures to return the magnetic flux. It is constituted by a barrel of 2.88 m thickness and 2 end-caps of 2.12 m thickness. Muon detectors are inserted inside the iron yoke in a sandwich-like structure. They're performing measurement on muons but they are also used as tail catchers, to improve the energy resolution of high energetic jets escaping the calorimeters.

2.4 Conclusions

In this chapter, the reasons to build a linear electron/positron collider were discussed by introducing the pros and cons of such a big experiment. In order to reduce the costs, only one interaction region is planned but two detectors are going to operate alternately. The design of the detectors is driven by the particle flow approach to reach a ... energy resolution. In particularly, the onion structure of ILD was peeled. The different sub-detectors and the technology options were introduced, except for the vertex detector. Indeed, the chapter 4 will be dedicated to the vertex detector at the ILD.

The next chapter will introduce the physics cases at the ILC, especially by describing an approach to a physics analysis to study the $H \to c\bar{c}$.

Chapter 3

Physics at the ILC

In the chapter 1, the framework of particles physics was described. Since the beginning of High Energy Physics, different experiments have been done to confirm the exactness of the SM but also to find new physics beyond the SM. The beam structure allow different kind of measurements. For example, the LHC has a high luminosity and high energy beam, able to reach new energy scale on earth, whereas the ILC is trying to reach more precise results, with less energy. This chapter will discuss the physics that will be studied at the ILC. It will focus particularly on the Higgs physics. An introduction to a physic analysis will be given.

Contents

3.1 Potential studies

As seen in chapter 2, the ILC will have a vast and variable tunable centre-of-mass energy. Due to the features of an e^+e^- collider, the initial state of collision is well defined. Contrary to the LHC, there are no strong interaction backgrounds and the electroweak background is controlled and calculable. This conditions will help to perform precise measurements and looking for new physics.

For example, the ILC will be able to collect more Z boson events than the LEP did at the centre-of-mass energy $\sqrt{2} = 91$ GeV. It will allow to perform ultra precise measurements of the Z boson and the electroweak sector to study the Z asymmetries and couplings, but also to measure rare processes that where limited by statistics at LEP.

By increasing the centre-of-mass energy to $\sqrt{s} = 160$ GeV, ultra precise measurements of the W mass could be performed (MeV precision) and with higher energy, it is also possible to measure precisely the W boson couplings. Also, at higher energy, there is a new perspective to measure precisely the nature of the Higgs boson and its coupling. The large statistics given by the ILC will permit to study rare Higgs decay.

Top physics

New physics

Energy (GeV)	Reaction	Physics Goal
91	$e^+e^- \to Z$	ultra-precision electroweak
160	$e^+e^- \to WW$	ultra-precision W mass
250	$e^+e^- \to Zh$	precision Higgs coupling
350 - 400	$e^+e^- \to t\bar{t}$	top quark mass and couplings
	$e^+e^- \to WW$	precision W couplings
	$e^+e^- \to \nu\bar{\nu}h$	precision Higgs couplings
500	$e^+e^- \to f\bar{f}$	precision search for Z'
	$e^+e^- \to t\bar{t}h$	Higgs coupling to top
	$e^+e^- \to Zhh$	Higgs self-coupling
	$e^+e^- \to \tilde{\chi}\tilde{\chi}$	search for supersymmetry
	$e^+e^- \to AH, H^+H^-$	search for extended Higgs states
700-1000	$e^+e^- \to \nu\bar{\nu}hh$	Higgs self-coupling
	$e^+e^- \to \nu\bar{\nu}VV$	composite Higgs sector
	$e^+e^- \to \nu\bar{\nu}t\bar{t}$	composite Higgs and top
	$e^+e^- \to \overline{tt}^*$	search for supersymmetry

Table 3.1 – Summary of the major processes that will be studied at the ILC for different energies[3].

h

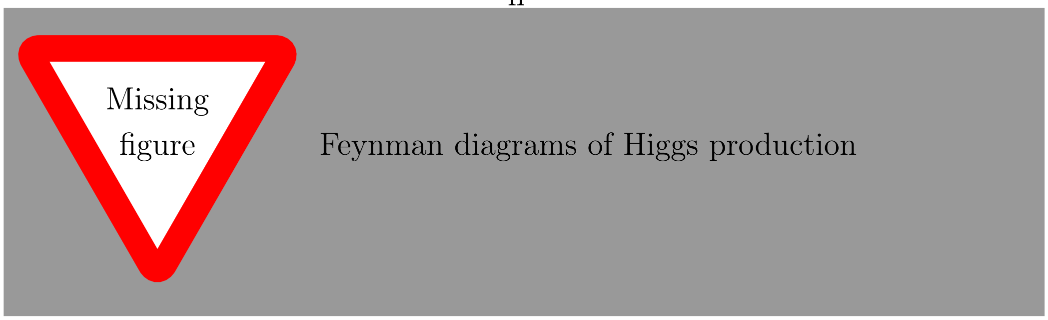

Figure 3.1 – The higgs production processes at the ILC.

3.2 Higgs physics

3.2.1 Production of the Higgs at the ILC

Contrary to the LHC, the Higgs will be accessible by direct measurement. They are three major processes Higgs boson production at the ILC, the Higgs-strahlung, the WW-fusion and the ZZ-fusion:

Higgs-strahlung: $e^+e^- \rightarrow ZH \rightarrow f\overline{f}X$

WW-fusion: $e^+e^- \rightarrow \nu\overline{\nu}W^+W^- \rightarrow \nu\overline{\nu}H$

ZZ-fusion: $e^+e^- \rightarrow e^+e^-ZZ \rightarrow e^+e^-H$

The Higgs-strahlung is a s-channel process that is dominant at 250 GeV and its cross-section falls off as 1/s as the centre-of-mass energy $\sqrt{s}$ increases. The WW-fusion and ZZ-fusion are t-channel processes. The cross-section grows logarithmically with the center-of-mass energy and the contribution of the fusion processes is small at 250 GeV.

The polarisation of the beam will help the experimenters to select Higgs reactions or to change the mixture of signal and background. For example, the WW-fusion occurs only with left-handed electrons associated to right-handed positrons.

The figure shows the cross-section production of the Higgs at the ILC regard to the energy of the collision. ADD REF TO THE FIGURE

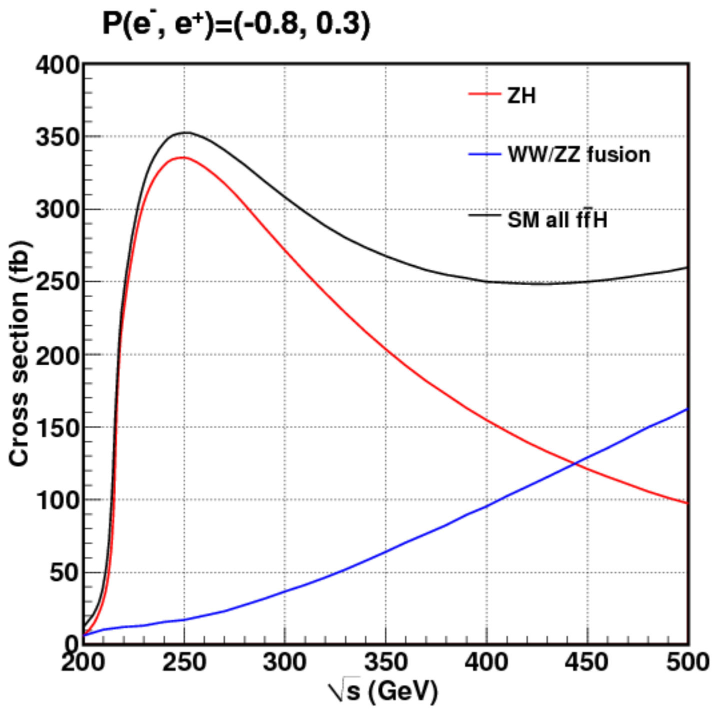

Figure 3.2 – The cross section production of the Higgs boson with a mass of 125 GeV. REF HIGGS WHITE PAPER

3.2.2 Decays of the Higgs

The Higgs boson couples to all the particles of the SM. There are many decay modes: $b\bar{b}$, WW, ZZ, gg, $c\bar{c}$, $\tau\tau$, $\gamma\gamma$, γZ At the LHC, the decay $h \to b\bar{b}$ can be observed with special kinematics but the $h \to c\bar{c}$ and $h \to gg$ decays are extremely challenging to observe.

3.3 Advantages of the ILC

The ILC has the main advantage to produce events non accessible at the LHC. Through this section, some benefits of the ILC are introduced thanks to a simple analysis of simulated data at 350 GeV.

The goal of this section is to present how to perform an analysis from simulated data. Measuring the Higgs coupling to $c\bar{c}$ is important to have a reference value to understand any deviations form the SM predictions in the Higgs coupling to $t\bar{t}$ and gg. To study this coupling, the analysis will be focus on the final state that gives two neutrinos and two jets coming from the Higgs.

3.3.1 Background processes

They are many background to take into account:

Chapter 4

Double-sided VXD: PLUME

Since en of the 1960's and the 1970's, the development of position sensitive silicon sensors has permitted to confirm the prediction of the Standard Model (SM) with a high precision, as well as the discovery of the t quark. These sensors, called Vertex Detector (VXD), are in charge to track the particles down to their decay vertices. The design of such device is held by the physics requirement of the experiment and is playing a crucial role at the International Linear Collider (ILC). For example, one flagship measurement is the study of the Higgs boson couplings to the fermions and other bosons. This can be achieved only with a precise heavy flavor tagging and the ability to separate the b quarks form the c quarks. Actually, the lifetime of the two quarks is close together (1.3^{-12} s for the b quark and 1.1^{-12} s for the c quarks), leading to a very close decay vertices.

Along this chapter, the role of the vertex detector and the physics requirements to build one suited for the ILC environment will be presented. Then, the different options of the International Large Detector (ILD) are shown, to focus on the double-sided ladders developed by the Pixelated Ladder with Ultra-low Material Embedding (PLUME) collaboration. To finish, the principle of Complementary Metal Oxide Semi-conductor (CMOS) sensors and their use in physics are described

Rewrite the introduction... It is not that great dude.

Contents

4.1 The ILD vertex detector specifications

The VXD is the closest sub-detector to the interaction point (IP) in charge of reconstructing the vertex by extrapolating particles back to their origin of production. This detector should be optimised to track particles in a high-density environment and to be able to extract the tracks from the different particles, especially the b and c quarks in the case of the ILC. The reconstruction of the displaced vertices should be efficient enough to perform a good flavour tagging. Therefore, the detector has to measure particles with a lifetime in the picosecond regime, representing a decay length between 150 and 500 μm. The minimum distance of the first VXD layer is determined by the beam pipe radius, and the background induced by beamstrahlung, to limit the pixel occupancy. This sub-detector has a central role in the track's reconstruction. Depending on the option chosen, the VXD has to provide five or six points of measurement with a very high precise spatial resolution. For the studies requiring vertex charge identification, it should be able to reconstruct low-momentum and very forward tracks.

4.1.1 Physics requirements

The ideal VXD should be made of sensors with a fine granularity in order to increase the ability to distinguish two nearest particles. The mechanical structure of the detector should provide a good stiffness and stability of the whole system but has to be at the same time as light as possible to reduce the interaction of the particles traversing it, before they reached another part of the main detector. As well, in order to reduce the unwanted interactions, the sensor technology used has to have a low power consumption to avoid any special cooling system which can have a bad impact on the material budget. The design of such detector, like the minimal distance of the first layer to the IP and the spacing between different layers, is determined by both the beam background and the physics to study. The flavour tagging ability, the vertex charge measurement and tracking, and the displaced vertices reconstruction are the main physics parameters driving the design. The distance of closest approach of a particle to the colliding beam is called the impact parameter and the resolution achievable by the detector is described by the formula 4.1[4].

$$\sigma_{IP} = a \oplus \frac{b}{p \sin \theta^k} \tag{4.1}$$

Where $k = \frac{3}{2}$ in the $R - \phi$ direction and $k = \frac{5}{2}$ in the z projection and θ the track polar angle.

The first term a is the impact parameter resolution of the sensors used for the VXD, which is linked up to the radius of the inner R_{int} and outer R_{ext} layers and the single point resolution $\sigma_{s.p.}$, as described in equation 4.2.

$$a = \sigma_{s.p} \frac{R_{int} \oplus R_{ext}}{R_{ext} - R_{in}} \tag{4.2}$$

In the case of the ILD, the single point resolution should not be higher than $\sigma_{sp} \simeq 3\mu$m, leading to an impact parameter with a resolution of the order of $a \simeq 5\mu$m.

The second term presented in the equation 4.3, is related to the multiple scattering inducing an incertitude on the impact parameter. It depends on the charge Z of the impinging particle, the material crossed by the particle $\frac{x}{X_0 \sin \theta}$ and the distance of the innermost layer to the IP. Depending on the momentum or the crossing angle of the incoming particles, the two parameters are more or less important. For low momentum particles or crossing particles with a shallow angle, the b parameter becomes important, while for higher momentum a dominates.

$$b = R_{int} \frac{13.6 MeV/c}{\beta c} Z \sqrt{\frac{x}{X_0}} \left[1 + 0.036 ln \left(\frac{x}{X_0 \sin theta} \right) \right] \tag{4.3}$$

For the ILC purpose, the ILD-VXD should reach an impact parameter resolution better than 5 μm and a b parameter better than 10 μm GeV/c. The values were never obtained before for other experiments. As a comparison, the resolution parameters for the LHC are: $a = 12$ μm and $b = 70$ μm GeV/c.

4.1.2 Design

REF Marcel VXD

The VXD is made of 12 cm long ladders arranged cylindrically in concentric layers to form long-barrels surrounding the IP, contrary to the SiD vertex detector with a design based on a 5 layers barrel, four endcap disks and three additional forward pixel disks.Two different geometries are competing for the ILC-ILD, nevertheless, they aimed to build long ladders. The first option is based on five single-sided layers with a material budget not exceeding 0.11 % of X_0 per layer. The five layers are in a radius range varying from 15 mm for the first layer to 60 mm for the last one. The second option is based on three double-sided layers. The material budget should be less than 0.16 % of X_0 for one detecting face. The mechanical structure, which holds the two layers, is 2 mm thick and will be in a radius range varying from 15 to 60 mm.

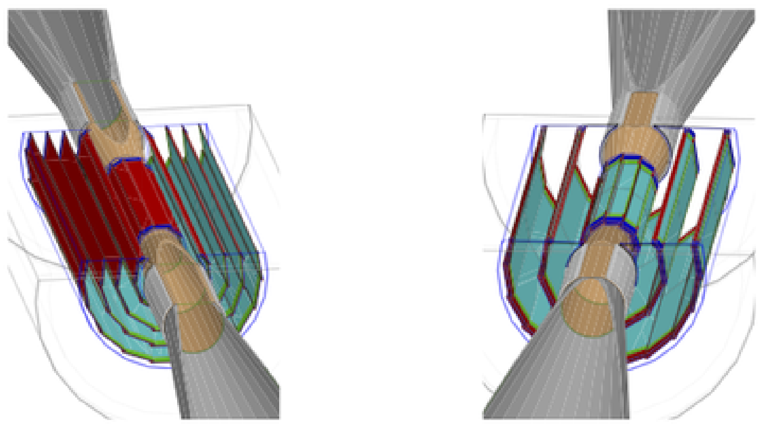

Figure 4.1 – Overview of the two vertex detector option for the ILC. On the left, it is made of five single sided layers, whereas the right one represents three double-sided layers.

Both geometry designs are based on pixel sensors instead of strips or any other silicon devices. A non-exhaustive list of the technologies under competition are presented below:

FPCCD

The Fine Pixels Charged Coupled-Device (FPCCD) [8] is based on the Charged Coupled-Device (CCD) processes. The sensor is using small pixels size (approximately $\sim 5\mu$m) to provide a sub-micron spatial resolution and an excellent capability to separate two nearby tracks. Its thickness is 50 μm and the epitaxial layer (15 μm thick) is completely depleted to limit the charge spreading around pixels and to reduce the number of hits per pixel. However, the CCD architecture provides slow readout and the matrix will be read between consecutive bunch trains, helping to reduce the power consumption and avoiding beam induced RF noise. At the moment, the FPCCD are operated at -40°C.

DEPFET

The Depleted P- Channel Field Effect Transistor (DEPFET) is a Active Pixel Sensor (APS) in which field effect transistors are incorporated into each pixel. The single point resolution is ~ 3 μm for pixels with a size of 20 μm. The silicon itself is used as sensitive part but also as a mechanical structure, minimising the support and services. The sensor is completely depleted of free charged carries thanks to a voltage applied along the thickness. The rolling-shutter approach is used for reading each row and the column readout is done by two auxiliary Application-Specified Integrated Circuits (ASICs).

REF for a DEPFET paper

CMOS

Different options for CMOS pixel sensors are studied, such as the 3D integrated CMOS, but due to the context of this thesis, the stress will be on the CMOS sensors based on the Minimum Ionizing MOS Active pixel sensor (MIMOSA) architecture developed by the IPHC of Strasbourg. This technology is described in section 4.3.

For all the technologies, the sensors' consumption has to be minimised in a way to reduce the cooling system and in the same time the added material budget in the sensitive detector volume. As it was shown on the figure 2.2 of the chapter 2, the bunch train will last less than 1 ms for a dead time of 200 ms. Two possibilities are envisaged to benefit from the beam structure. The first one consists to store the hits information thanks to a time stamp during the bunch crossing and to read out the data after the last collision. This method might be used by the FPCCD technology due to the slow integration time of the CCD. Another solution is to use a power-pulsing. Right after the last collision, the sensors are switched off or the power consumption is reduced as mush as possible, and before the first collision, the sensors is switch on again. This pulsing method is studied by different collaborations.

Another aspect not discussed yet is the radiation tolerance of the detector, which is directly related to the beam background. The first layer is the one the most affected by the background and it should have a high radiation tolerance. The required radiation tolerance is about 1 kGy for the total ionising dose and a fluence of $10^{11}\mathrm{n}_{eq}/\mathrm{cm}^2$[6].

The efficiency of the VXD has also to be excellent in order to maximise the tracking performances. The efficiency is defined here as the ratio of detected particles over all the particles crossing the detector. If one layer of the vertex detector misses a hit, the track reconstruction will be less accurate

Cooling system, integration time, radiation tolerance, electromagnetic interference

To summarise, the expected parameters expected for the ILC are:

- An excellent impact parameter resolution: $a \sim 5\mu$m and $b \sim 10\mu$m
- A material budget not exceeding 0.1 % X_0 per layer for the single-sided option (0.16 % X_0 for the double one)
- Radius of the first layer $\sim 15/16$ mm

4.2 PLUME

The Pixelated Ladder with Ultra-low Material Embedding (PLUME) project aims to produce double-sided ladder prototypes with respect to the ILC requirements. Three labs in the Europe are involved: the IPHC-PICSEL in Strasbourg, the University of Bristol and the DESY in Hamburg. The collaboration is studying the feasibility to build such vertex detector using MAPS thinned down to 50μm and is exploring the benefits of this design. Strasbourg is in charge to develop and mount the sensors on the modules, to take care of the readout and the Data AcQuisition (DAQ), and to provide a cooling system. The mechanical design, stability measurements and building the ladders are done by the University of Bristol, while DESY has studied the ladder mock-up, performed some power-pulsing tests and is now characterising and validating the modules in the lab. In 2016, the DESY has provided the opportunity to test the ladder in real conditions thanks to the test beam facility and the possibility to use the DAQ software developed at DESY: EUDAQ.

4.2.1 Design and goals

The figure 4.2 illustrates the design of a PLUME ladder. The ladder structure is defined by the sensors arrangement on the mechanical structure (positioned next to each other). In this design, the stiffener is a 2 mm thick Silicon Carbide (SiC) foam which has a density varying between 8% and 4% and could be reduced to only 2-3%. The choice of this foam is a good compromise between the stiffness and the thickness compare to other materials. The figure 4.3 is representing the structure of this foam. It is macroscopically uniform and has the advantage to be easily machinable. Nevertheless, it has a low thermal conductivity (50 W/m/K) and can't be used to dissipate the heat. On each side, a low mass flex-cable is glued, which is used to connect the sensors for powering and managing them. It is made of copper traces coated in Kapton, but new prototypes using aluminum traces are developed and currently tested in order to reduce the material budget. The ladder embeds twelve sensors, six on each face, that are glued and connected to the flex cable. On one edge of the flex-cable, a single Zero Insertion Force (ZIF) connector is used to link the ladder to the external board servicing, via a jumper cable. For the moment, the design is dedicated to the MIMOSA-26 sensors thinned down to 50μm but it can be adapted to any kind of MAPS sensors having the same thickness. Although the MIMOSA-26 has a spatial resolution better than 3μm (see subsection 4.3.4), the integration time is not suited for the bunch train structures of the ILC.

REF Joel paper

The aims of the collaboration are to build ladders with a material budget better than 0.35% of X_0 for a spatial resolution better than 3μm, and thus to evaluate the benefits of a double-sided measurement.

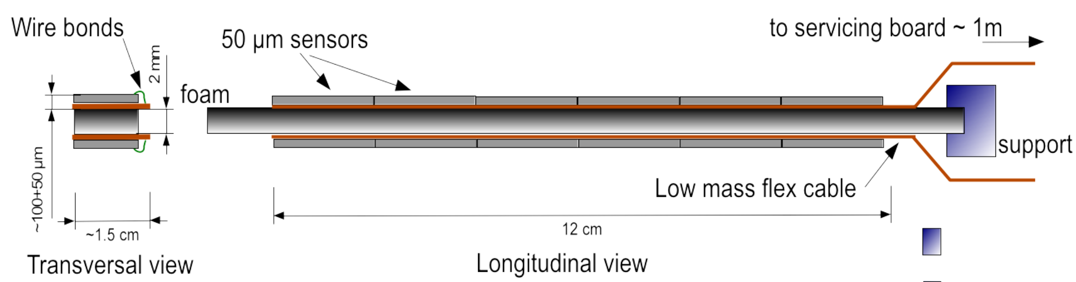

Figure 4.2 – Side view (transversal and longitudinal) of the PLUME mechanical structure.

4.2.2 Prototypes

Since 2009, the collaboration is studying the design, the production, the impact of the mechanical structure on the ladder's performances, but also

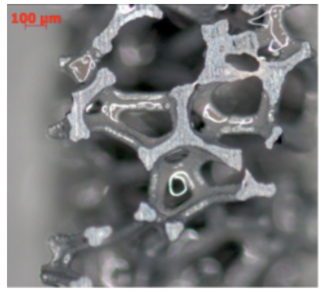

Figure 4.3 – Microscopical view of the silicon carbide foam structure.

how to power and control the sensors together. The first ladder prototype, called version-0 (V-0) was developed and tested in 2009. The purpose of this prototype was to settle the fabrication and the test beam procedures, without trying to reach the desired material budget goal. Two MIMOSA-20 analog output sensors were mounted on each side of a stiffener, providing a 1×4 cm^2 sensitive area. The prototype was tested in 120 GeV pion beam at the CERN-SPS and the results have demonstrated the benefits of the double-sided measurement on the spatial resolution, which is improved by about 25%[23].

Then in 2010, a second prototype featuring a design closer to the wanted goal, called version-1 (V-1), was developed. Each module of the ladder was made of Kapton flex-cable with a thickness of 0.14 mm, using copper traces. They are denoted Optiprint-Kapton-Flex-cable (OKF), where Optiprint is the vendor of these flex-cable. It is the first version to embed six MIMOSA-26 binary output sensors working simultaneously on each side of the stiffener. The material budget is estimated to be 0.65 % of X_0 in the sensor's sensitive area. The aim of this prototype was to validate the operation of multiple sensors in a chain. Two ladders were tested in real conditions. The first one was tested with 120 GeV pions at CERN-SPS in 2011, while the second ladder was tested in April 2016 with up to 5 GeV positrons at DESY in Hamburg. The DESY test beam results are presented in chapter ???, while a specific study of the sensor's deformation observed at CERN is discussed in chapter ???.

At the beginning of 2016, the third prototype versions were mounted but have not yet been completely tested. In fact, this new version is divided into two sub-versions: one using copper traces and the other one aluminum traces. Nevertheless, both sub-versions have a new design featuring reduced traces thickness to have a narrower flex-cable (18 mm width) adjusted to the sensors width in order to minimise the dead areas. The flex-design has

Figure 4.4 – Front view of the ladder version-1 made in 2010 in its holding box. On the left, there is the connector to the output board servicing, on the right a connection to blow air on the module. As this version was not made with a mirrored design, the flex-cables are not entirely overlapping and the SiC foam can be seen (in black here).

slightly changed to have a mirrored geometry in order to minimize the dead area too and have a better alignment solution. The stiffener is made of a lower density SiC foam reducing the global material budget.

The table 4.1 summarises the material budget reached by the different prototypes.

4.2.3 Perspectives

Although the collaboration has shown their expertise to build light mechanical structures, more tests and optimisations have to be done. MIMOSA-26 sensors are not designed to match the ILC specs. The integration time of this sensor is 115.2 μs, whereas the bunch train last only 0.95 ms (bunch crossing spaced out by 337 ns), a new CPS with a faster integration time has to be integrated. Another problem of the MIMOSA-26 sensors is that they are not suited for a power pulsing. As a reminder, the principle of the power pulsing is to reduce the consumption of the sensor during the 200 ms

Layer	budget (% X_0)		
	V-0	V-1	Goal
Sensor	0.053	0.053	0.053
Flex-cable	0.524	0.150	0.034
Passive components	0	0.033	0.033
Stiffener (foam)	0.764	0.175	0.087
Total	1.926	0.654	0.334

Table 4.1 – Estimation of the material budget for the different prototypes of the PLUME ladder.

dead time. Nevertheless, a power-pulsing study on a single Mi-26 sensor has been done and the results have shown that the nominal supply voltage of the MIMOSA-26 can be lowered from 3.3 V to 1.85 V without losing the sensor's registers. The fake hit rate measured was close to the one obtained in normal conditions after the sensor reaches a stable operation. Moreover, the power consumption was reduced by a factor 6.34[18].

A complete power-pulsing study of the whole ladder in the lab has to be done in order to make sure that the sensors are still behaving correctly. If the first results are comforting, the power-pulsing will be tested under real conditions with a high magnetic field. The impact of the Lorentz forces due to the coupling of the power-pulsing and the magnetic field is going to be studied, especially is this structure will induce unwanted deformations or vibrations.

The collaboration is considering to embed the sensors directly inside the multi-layer micro-cable[5]. The chips are glued on the first polyimide substrate layer, then the metal layer is deposited on top of it and the metal traces are directly connected to the chips pads. Then an insulator is added to the module. The advantages of this technique are, firstly, the direct connection of metal traces to the pads that avoid wire-bonding and can reduce, in the same time, the width of the module. And secondly, this structure has the advantage to apply the mechanical stress on the polymer wrapping, thus reducing it on the sensor.

A closer perspective for the collaboration is to integrate two ladders in the physics commissioning of the BEAST experiment at KEK. The version-2 ladder will be used but a second option is foreseen. MISTRAL sensors will be mounted on the flex-cable instead of the MIMOSA-26. These sensors have a bigger sensitive area, a faster integration time ($\sim 20\mu$s) but a worth spatial resolution ($< 10\mu$m) due to the pixel size (pitch of 36x62.5μm^2).

4.3 Integration of CMOS sensors

The PICSEL group of the IPHC at Strasbourg is developing since 1999 CMOS sensors called MIMOSA for *Minimum Ionizing MOS Active pixel sensor*. They are semi-conducting pixel sensors based on the APS, an alternative to the CCD developed at the beginning of the 1990's by the imaging industry and used nowadays for the smartphone's cameras. One particularity of the sensors developed by Strasbourg is that the different region of the CMOS, such the sensitive area or the electronic layer where the signal is processed, are made of the same material. This device is called then Monolithic Active Pixel Sensor (MAPS) and the different layers are:

- A substrate providing a mechanical stability;
- An epitaxial layer which is the sensitive volume of the sensor;
- An electronic layer where are located the diodes collecting the charges and the microelectronic processing the signal.

The motivation to use this technology or any other silicon sensor in particle physics is due to the minimum energy needed to create an electron/hole pair by a traversing particle. In silicon, this minimum energy is only 3.6 eV, while for a gaseous detector, it is close to 30 eV.

4.3.1 Charges creation and signal collection

The CMOS sensor can detect crossing particles thanks to their structure, but also to the interaction of particles with matter. When a particle is traversing a layer of matter, it loses energy via interactions with electrons and nuclei. Due to the size of a MAPS, it loses only a small fraction of its energy, and the energy loss can be described by a Landau. A Minimum Ionizing Particle (MIP), creates 80 electrons per microns inside the silicon.

At the beginning, the microelectronic industry has insulated the transistors from the substrate thanks to a high resistivity layer, called the epitaxial layer. The development of CMOS sensors was done thanks to the properties offered by these semiconductors.

The CMOS sensors developed by the IPHC at Strasbourg are called monolithic MAPS sensors because the different layers of the sensor are made in one block of the same material, but with different doping. The structure of the sensor is a highly doped P+ substrate made of a moderate quality silicon.

The crystal structure contains a lot of defects, hence the recombination rate of charge carriers is high. Above the bulk, a low doped P- layer is grown. The silicon used has a good quality, thus the charge carriers have less change to recombine. It is the sensitive part of the sensor and is called the epitaxial layer. On top of it, an N-well implant has the role of the charge collection. The interface between the N-wells and the epitaxial layer forms a P-N junction, called a collection diode. A depleted area is created by this junction, on which the charge carriers are attracted. Nevertheless, this P-N junction is only one part of the pixel. Next to the N-well implants are sitting highly doped P-well in charge to reflect the charge carriers to the implants. The difference of doping between the bulk and the epitaxial layer is also used to reflect the charge carriers to the collection diode.

The typical doping concentration are 10^{15}at/cm^3 for the epitaxial layer, 10^{19}at/cm^3 in the substrate and 10^{17}at/cm^3 for the other layers. The doping concentration defines the size of the depleted region. For this doping concentrations, only a small region around the P-N junction is depleted, while the epitaxial layer is mainly undepleted.

As no external voltage is applied to the sensor to increase the depleted region, the charge carriers created by crossing particles are thermally diffused inside the epitaxial layer to the diode. Nevertheless, the different doping levels produce a built-in voltage defined as:

$$V_b = \frac{kT}{q} ln\left(\frac{N_{p+}}{N_{p-}}\right) \tag{4.4}$$

The built-in voltage depends on the Boltzmann constant k, the temperature T, the elementary charge q and the different concentrations doping $N_{p\pm}$ of the interface. Due to the different doping levels, the electrons are restricted to diffuse inside the sensitive volume, to be then guided towards a collection diode. One effect of the thermal diffusion is that the average path of the electrons in the epitaxial layer is longer than the one they would have in a fully-depleted sensor. Hence, the probability of recombination between an electron and a hole is increasing. Also the charges tend to spread more around neighboring n-well. Therefore, the charge collection efficiency is lower than the fully-depleted sensor.

4.3.2 Pros and cons of the technology

The CMOS sensors have several interesting properties. First of all, the fabrication cost is lower than other pixel technologies due to the industrial pro-

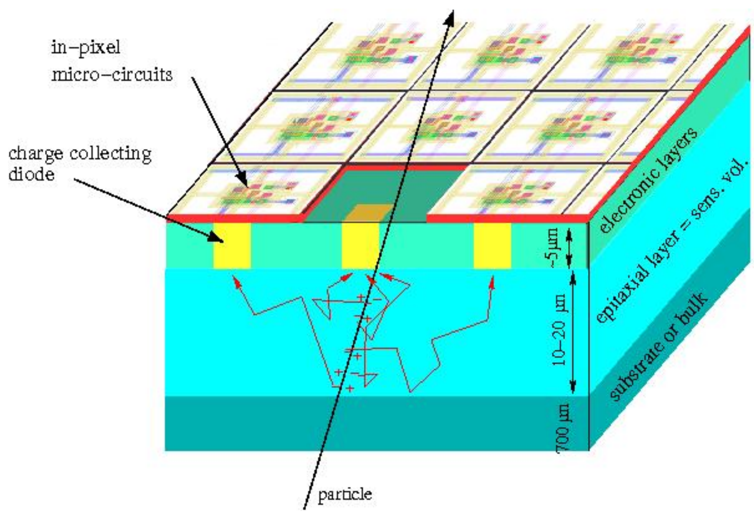

Figure 4.5 – Drawing of MAPS structure representing the different layers of the sensor and the path of charge carriers in the epitaxial layer.

cesses used to build the sensors. Therefore, many prototypes and bigger matrices can be built, while benefiting from the industrial experience. For example, the imaging industry has developed smaller and smaller grid size and a pitch size of ten microns can be achieved.

Secondly, due to the size of the depleted area, the charge carriers tend to spread more over neighbouring pixels. On the one hand, the signal collected per pixel is smaller, but on the other hand, the reconstruction of the hit position with a centre of gravity algorithm is improving the spatial resolution. To give an idea, a binary output sensor with a pitch of 18.4 μm can achieve a spatial resolution better than 3 μm.

Thirdly, the distinct doping of the different layers is responsible for the reflection of the charge carriers to the collection diodes. However, only the interface between two different doped regions is responsible for this reflection. Thus, the substrate can be thinned down to few microns leading to a sensor with a thickness of 50 μm, while keeping the possibility to manipulate them. In this way, the material budget can be reduced down to 0.053% X_0.

Nevertheless, the thickness of the epitaxial layer (usually between 10 and 15μm) and the small depleted region are responsible for a small charge collection. As a matter of fact, a MIP is creating 80 electron/hole pairs per microns, so the number of charges collecting by the diode is of the order of a thousand electrons. Hence, the signal created is only few millivolts and low noise electronics have to be used for processing the signal.

CMOS sensors are sensitive to ionizing and non-ionizing radiations that degrade the sensor properties. The non-ionizing radiations are damaging the crystal structure of the epitaxial layers, creating defaults in the lattice. The recombination rate is increasing and reduces the signal collected. To avoid this effect, two solutions are possible. The first one is to reduce the size of the pixels in order to decrease the path of the particles from the epitaxial layer to the collection diodes. Nevertheless, the cost to build sensors with a smaller pitch is increasing. The second solution is to increase the resistivity of the epitaxial layer to expand the depleted area.

The ionizing radiations are responsible for charges accumulation in the electronic layer. The leakage current is increasing in the pixel and diode collection. To reduce the leakage current, smaller diodes can be used to reduce the impact of the leakage current but as it was explained before, the cost of fabrication is increasing.

4.3.3 Signal processing

If no charge is collected by the pixel, the voltage at the equivalent capacitor of the diode is evolving because of the leakage current inherent in the junction. The pixel reading can be done in two different ways, depending on the method used to minimise the leakage current effect. Currently, two pixel's architectures are used to compensate the diode's leakage current: the *3 Transistors pixel design*, mainly used in imaging, and the *self-biased pixel design*. The circuit diagram which is shown on the figure 4.6 represents the two methods to design pixel.

The first one, presented on figure 4.6a, consists to reinitialise the collection diode's voltage to a reference voltage thanks to a *reset* transistor, denoted M1 on the diagram. This method works in two steps. Firstly, the M1 transistor is closed and the charge of the equivalent capacitor C_d associated to the junction P-N, represented by a diode on the diagram, is slowly decreasing because of the diode's leakage current. During this phase, the pixel is sensitive and is read. After a time interval equivalent to the integration time of the sensor, the transistor M1 is opened to recharge C_d to its initial voltage. During this time, the pixel is not sensitive. While M1 is used for the reset, M2 is used as a pre-amplifier of the signal created by the diode and M3 link up the voltage to the output of the circuit. Although this compensation method is fast, it generates a dead time for detection between two readings.

The figure 4.6b depicts the *self-biased pixel design* method[11]. It is using a P-N junction (symbolised here by a diode mounted on the other side) coupled to the N-well implant to absorb the leakage current. The inverted diode is continuously compensated the diode's leakage current, thus the dead time is vanished. While no particle is crossing the sensor, an equilibrium appears between the leakage and recharge current. A particle going through the sensor disrupts this equilibrium. The charges collected by the pixel lead to a discharge of the diode's capacitor C_d, followed by a recharge of this capacitor thanks to the second diode to reach again the equilibrium. Nevertheless, if the recharge procedure is too fast compare to the integration time, the physics signal is masked and the passage of the particle is never notified. Even if the time interval to recharge the capacitor C_d is set properly, an important charge collection per pixel could disturb the recharge phase and the pixel will reach a stable level again only a long time interval of the order of 10 ms.

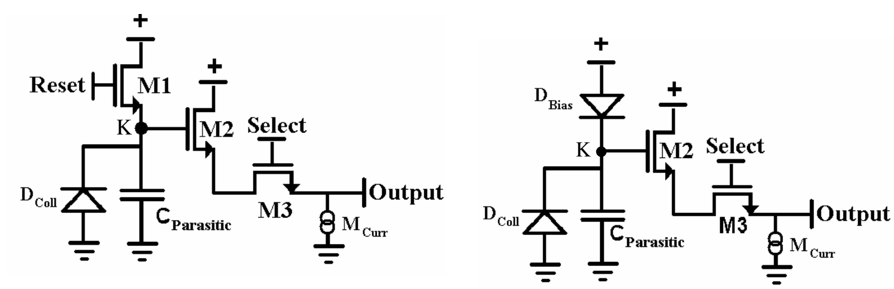

(a) Three transistors (3T) pixel design.

(b) Self-biased pixel design.

Figure 4.6 – Two different architectures of pixel.

Integration time and readout

For a non-depleted epitaxial layer, the charge carriers are thermally diffused to the collection diodes. The time to collect these charges in a pixel is ~ 100 ns, setting a maximal limit to read the signal. This integration time is not reachable due to other factors, like the pixel occupancy or the time needed to obtain the information of all the pixels. Also, a compromise to reach fast integration time has to be done. Faster is the sensor, more important is the power consumption of the electronic. Moreover, to reduce the integration time, a solution consists to increase the size of the pixels. In consequence, the pointing resolution of the device is impacted. For the case of the ILC, the integration time is dictated by the pixel occupancy that should not be bigger than a percent, to stay in the using sensor's range and to be able to reconstruct the impact.

The first sensors developed were using an analog output. With this approach, the pixels were addressed sequentially and their output was multiplexing in one bus line. The advantage of such method is that the discrimination can be adjusted offline for each pixel, thus compensating the non uniform response. Nevertheless, the integration time is depending on the operational frequency of the bus (usually 50 MHz) and the number of pixels contained in a matrix. For a sensor having millions of pixels, the integration time is then of the order of the millisecond. An analog output is then too slow for an ILC purpose.

To overcome this problem, an approach is to group the pixels in columns and to read them in parallel. The figure 4.7 depicts the principle of this method called *column parallel readout* or *rolling-shutter*. Instead of having one bus line for the whole matrix, each columns has in own bus and a data sparsification logic is integrated on the periphery of the sensor. One row is read in only 100 ns, independently of the number of pixels contained. When one line is read, the precedent line is processed by the electronics on the bottom each columns. Only the pixels having a signal above a certain thresholds are read. A zero suppression logic, called Suppression de zéro (SUZE), is in charge to determine the number of fired pixels in a raw and to send the address of the first pixel hit, as shown on figure 4.8.

- Digital output with zero suppression is decreasing data band-with and readout
- Rolling-shutter: read one line one the previous line is treated. => One row read in 100 ns independently of the number of columns
- Presentation of SUZE

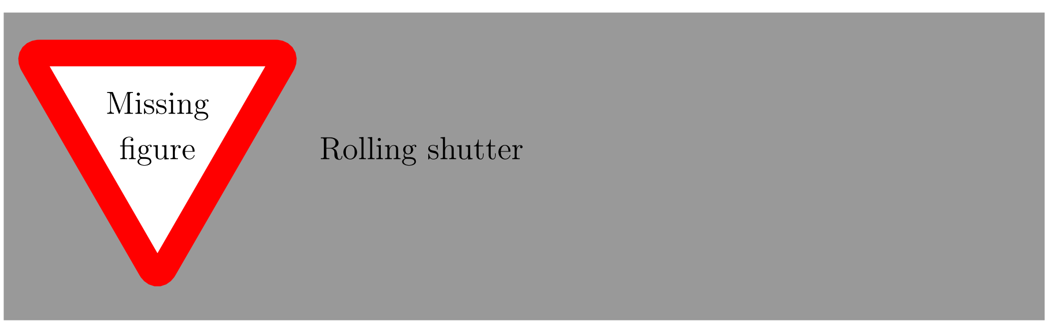

Figure 4.7 – Parallel column readout.

Figure 4.8 – Zero suppression principle.

Noise

Fixed Pattern Noise (FPN) and Temporal Noise (TN)

Noise during reset : correspond to TN, only for 3T pixels induced by

Noise during integration : shot noise, leakage current fluctuations, leakage current (process, temperature, architecture)

Noise during readout

Correlated Double Sampling : done inside a pixel or at the end of a column. Remove FPN and reset noise

The chapter 5 describes the steps to characterise the fixed pattern noise and temporal noise.

4.3.4 State of the art in high energy physics

The PICSEL group has developed sensors, called or ULTIMATE, for the STAR experiment at Brookhaven National Laboratory. They are based on MIMOSA-28 sensors and are integrated into the vertex detector. The figure 4.9 is showing a half-section of the STAR vertex detector (subfigure 4.9a) and a MIMOSA-28 bounded on a PCB. The choice for this technology was made because of their characteristics. Indeed, the thickness of a sensor is around 50 μm in order to minimise the multiple scattering of particles. The matrix is made of roughly 9×10^5 pixels, corresponding to 960 columns and 928 rows for a pitch of 20.7 x 20.7 μm^2. The sensitive area is 19.7 x 19.2

REF to a paper

cm^2. They have a binary output integrating a zero suppression technology (SUZE) and the integration time of the whole matrix is 200 μs. Thanks to this architecture, the sensors can reach a particle detection rate of 10^6 particles/cm^2/s. Finally, their power consumption is lower or equal to 150 mW/cm^2. The spatial resolution obtained for ULTIMATE is less than 4 μm.

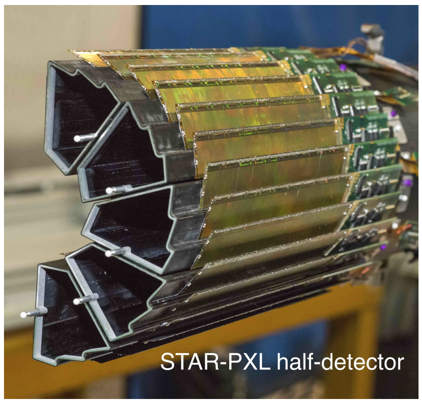

(a) Half part picture of the pixel vertex detector at STAR.

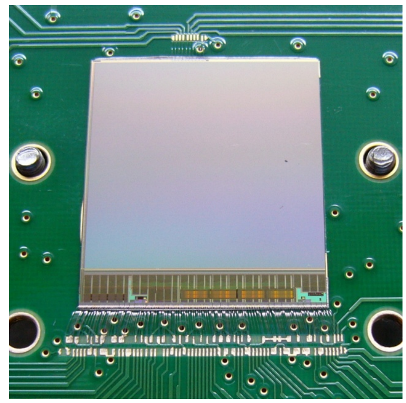

(b) ULTIMATE chip bounded on a PCB. The top wire bounds are used for a slow analog output dedicated to lab test, while the bottom ones are the wire bounds which control and read the sensor.

Figure 4.9 – Pictures of the STAR vertex detector and an ULTIMATE chip

An older version of the MIMOSA-28, based on the same architecture is currently used on the PLUME ladder: MIMOSA-26. Contrary to his brother, the matrix contains roughly 7×10^5 pixels, distribute on 1152 columns and 576 rows. The pixels are scared with a pitch of 18.4 μm and the sensitive area is 21.2 x 10.6 cm^2. They also have a binary output integrating a zero suppression mode but the integration time of the whole matrix is 115.2 μs. The architecture of a MIMOSA-26 is represented on figure 4.10. The power consumption is 1.1 μW/pixel. These sensors are equipping the telescope planes at DESY and CERN.

Figure 4.10 – Layout of the MIMOSA-26 matrix.

Chapter 5

Electrical Validation and laboratory testing

This chapter is introducing the steps to characterise and validate a sensor in lab before testing it in real conditions.

- Describe bench
- Describe control of a sensor
- Describe output of Mi-26

5.1 Mechanical check

- Check positioning matrix defect (crack)
- Check wire bounds
- Check alignment

5.2 Electrical validation

- Check consumption
- Check JTAG control
- Check Output

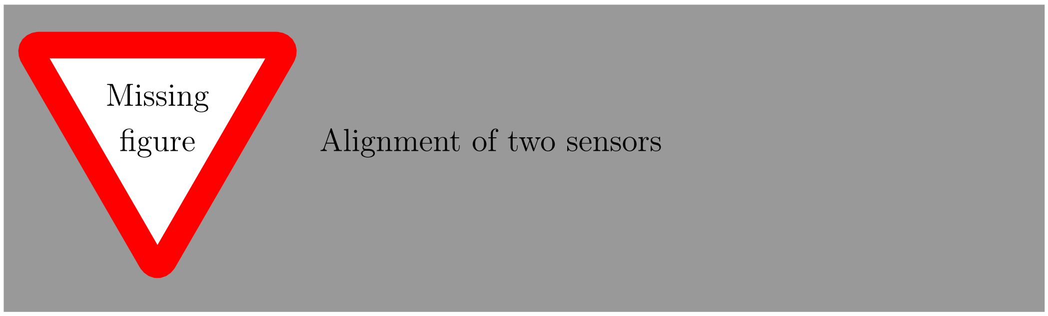

Figure 5.1 – Alignment check made with a microscope.

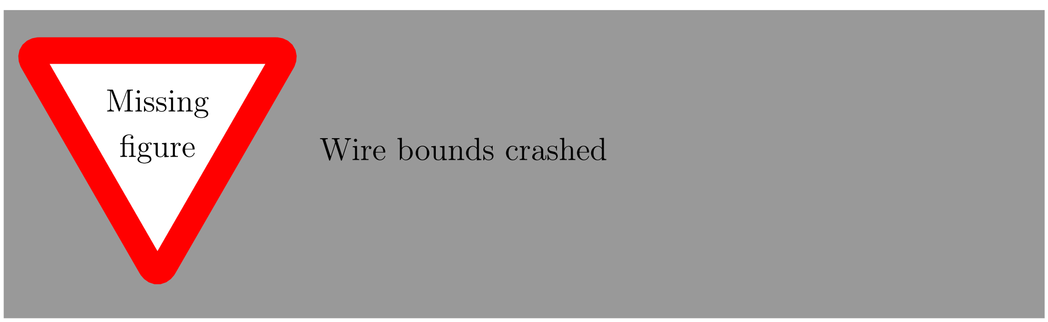

Figure 5.2 – One has to be careful!

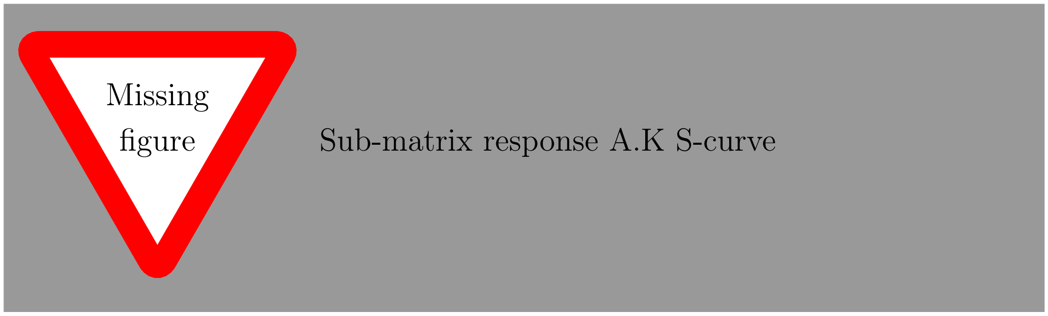

Figure 5.3 – Sub-matrix response

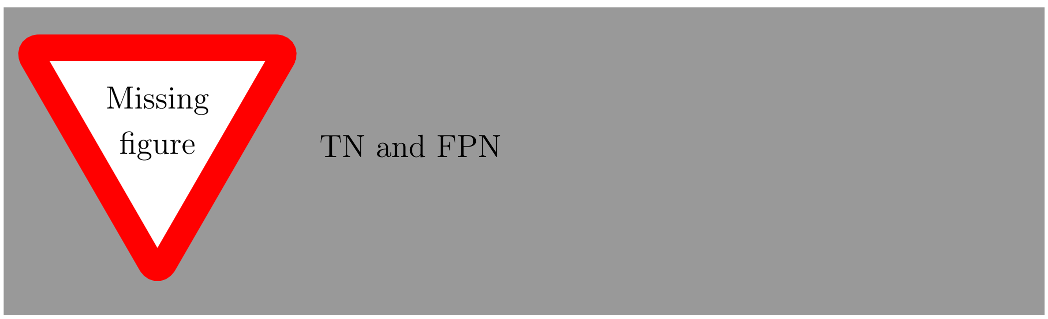

Figure 5.4 – TN and FPN

5.3 Noise estimation

- Describe steps
- Describe analysis
- FHR with normal acquisition

5.4 Cluster

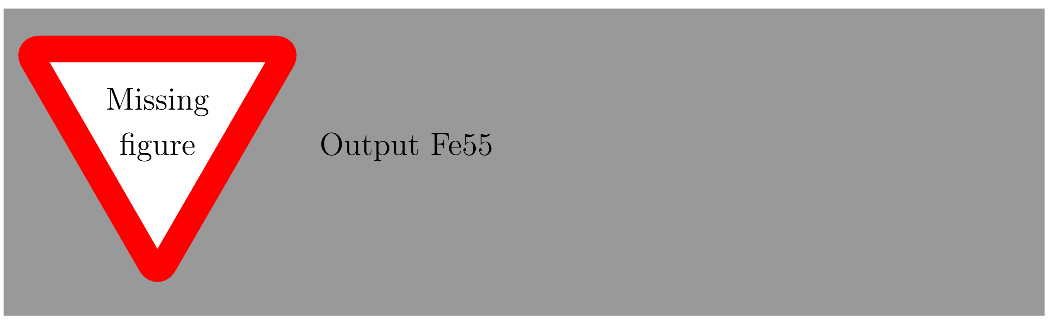

Figure 5.5 – Output of 10k events acquisition with a Fe55 radiation source.

Chapter 6

Test beam analysis

6.1 Experimental set-up

6.2 Deformation studies

6.3 Benefits of double-point measurements

Acronyms

AHCAL Analogue HCAL. 36

APS Active Pixel Sensor. 49

ASIC Application-Specified Integrated Circuit. 49

BDS Beam Delivery System. 25

CCD Charged Coupled-Device. 48

CLIC Compact LInear Collider. 24

CMOS Complementary Metal Oxide Semi-conductor. 45

DAQ Data AcQuisition. 50

DC Direct-current. 25

DEPFET Depleted P- Channel Field Effect Transistor. 49

ECAL Electromagnetic CALorimeter. 33

EM electromagnetic interaction. 3

ETD End-cap Tracking Detector. 33

FPCCD Fine Pixels Charged Coupled-Device. 48

FPN Fixed Pattern Noise. 61

FTD Forward Tracking Detector. 33

GRPC Glass Resistive Plate Chamber. 36

HCAL HAdronic CALanalogue HCALorimeter. 35

ILC International Linear Collider. 24

ILD International Large Detector. 21

IP interaction point. 28

IR interaction region. 25

LHC Large Hadron Collider. 21

LHCAL Low angle Hadron CALorimeter. 36

MAPS Monolithic Active Pixel Sensor. 35

MIMOSA Minimum Ionizing MOS Active pixel sensor. 49

MIP Minimum Ionizing Particle. 55

OKF Optiprint-Kapton-Flex-cable. 52

PFA Particle Flow Algorithm. 29

PLUME Pixelated Ladder with Ultra-low Material Embedding. 45

RTML Ring To the Main Linac. 26

SDHCAL Semi-Digital HCAL. 36

SET Silicon External Tracking. 33

SiC Silicon Carbide. 51

SiD Silicon Detector. 29

SIT Silicon Internal Tracker. 33

SM Standard Model. 2

SRF Superconducting Radio-Frequency. 24

SUZE Suppression de zéro. 60

TN Temporal Noise. 61

TPC Time-Projection-Chamber. 30

VXD Vertex Detector. 32

ZIF Zero Insertion Force. 51

Bibliography

[1] Georges Aad et al. Observation of a new particle in the search for the Standard Model Higgs boson with the ATLAS detector at the LHC. *Phys. Lett.*, B716:1–29, 2012.

[2] R. Appleby, L. Keller, T. Markiewicz, A. Seryi, R. Sugahara, and D. Walz. The International Linear Collider Technica. 3, 2006.

[3] H Baer, T Barklow, K Fujii, Y Gao, and a Hoang. [1306.6352] The International Linear Collider Technical Design Report - Volume 2: Physics. *... preprint arXiv:13066352*, 2, jun 2013.

[4] M. Battaglia. Vertex tracking at a future linear collider. *Nucl. Instruments Methods Phys. Res. Sect. A Accel. Spectrometers, Detect. Assoc. Equip.*, 650(1):55–58, sep 2011.

[5] Jerome Baudot, Olena Bashinska, Nathalie Chon-Sen, Wojciech Dulinski, Franziska Hegner, Marie Gelin-Galibel, Rhorry Gauld, Mathieu Goffe, Joel Goldstein, Ingrid Gregor, Christine Hu-Guo, Ulrich Koetz, Andrei Nomerotski, and Marc Winter. Development of Single- and Double-sided Ladders for the ILD Vertex Detectors. mar 2012.

[6] T. Behnke, J. E. Brau, B. Foster, J. Fuster, M. Harrison, J. P. Paterson, M. Peskin, M. Stanitzki, N. Walker, and H. Yamamoto. ILC Technical Design Report Volume 1: Executive Summary. *ILC Tech. Des. Rep. Vol. 1 Exec. Summ.*, 1:1–60, 2013.

[7] Ties Behnke. The international linear collider. *Fortschritte der Phys.*, 58(7-9):622–627, 2010.

[8] Constantino Calancha Paredes, A Dubey, H Ikeda, A Ishikawa, S Ito, E Kato, A Miyamoto, T Mori, H Sato, T Suehara, Y Sugimoto, and H Yamamoto. Progress in the development of the vertex detector with fine pixel CCD at the ILC.

[9] Serguei Chatrchyan et al. Observation of a new boson at a mass of 125 GeV with the CMS experiment at the LHC. *Phys. Lett.*, B716:30–61, 2012.

[10] Deutsches Elektronen-synchrotron Desy and Hamburg Germany. A review of e+ e- Linear Colliders. 22:529–539, 1988.

[11] M Deveaux, S Amar-Youcef, A Besson, G Claus, C Colledani, M Dorokhov, C Dritsa, W Dulinski, I Fröhlich, M Goffe, D Grandjean, S Heini, A Himmi, C Hu, K Jaaskelainen, C Müntz, A Shabetai, J Stroth, M Szelezniak, I Valin, and M Winter. Radiation Tolerance of CMOS Monolithic Active Pixel Sensors with Self-Biased Pixels. 2009.

[12] F. Englert and R. Brout. Broken Symmetry and the Mass of Gauge Vector Mesons. *Physical Review Letters*, 13:321–323, August 1964.

[13] E. Fermi. An attempt of a theory of beta radiation. 1. *Z. Phys.*, 88:161–177, 1934.

[14] R. P. Feynman and M. Gell-Mann. Theory of the fermi interaction. *Phys. Rev.*, 109:193–198, Jan 1958.

[15] Steven Green, John Marshall, Mark Thomson, and Boruo Xu. Cambridge linear collider group - home page. http://www.hep.phy.cam.ac.uk/linearcollider/calorimetry/.

[16] Peter W. Higgs. Broken symmetries and the masses of gauge bosons. *Phys. Rev. Lett.*, 13:508–509, Oct 1964.

[17] ICFA. Final International Technology Recommendation Panel Report. (September), 2004.

[18] Oleg Kuprash. Power pulsing of the CMOS sensor Mimosa 26. *Nucl. Instruments Methods Phys. Res. Sect. A Accel. Spectrometers, Detect. Assoc. Equip.*, 732:519–522, 2013.

[19] T. D. Lee and C. N. Yang. Question of Parity Conservation in Weak Interactions. *Physical Review*, 104:254–258, October 1956.

[20] Yiming Li, Chris Damerell, Rui Gao, Rhorry Gauld, Jaya John John, Peter Murray, Andrei Nomerotski, Konstantin Stefanov, Steve Thomas, Helena Wilding, and Zhige Zhang. ISIS2: Pixel Sensor with Local Charge Storage for ILC Vertex Detector. page 11, jun 2010.

[21] Ronald Lipton. Muon Collider: Plans, Progress and Challenges. page 6, apr 2012.

[22] O. Markin. Backgrounds at future linear colliders. feb 2014.

[23] A Nomerotski, L Bachynska, J Baudot, N Chon-Sen, G Claus, R De Masi, M Deveaux, W Dulinski, R Gauld, M Goffe, J Goldstein, I.-M Gregor, Ch Hu-Guo, M Imhoff, U Koetz, W Lau, C Muntz, C Santos, C Schrader, M Specht, J Stroth, M Winter, and S Yang. PLUME collaboration: Ultra-light ladders for linear collider vertex detector.

[24] K. A. Olive et al. Review of Particle Physics. *Chin. Phys.*, C38:090001, 2014.

[25] Adrian Signer. ABC of SUSY. *Journal of Physics G: Nuclear and Particle Physics*, 36(7):073002, jul 2009.

[26] C. S. Wu, E. Ambler, R. W. Hayward, D. D. Hoppes, and R. P. Hudson. Experimental Test of Parity Conservation in Beta Decay. *Physical Review*, 105:1413–1415, February 1957.